SPIN-UP OVER STEEP TOPOGRAPHY AND THE EFFECTS OF A SUBMARINE CANYON

by

Ramzi Mirshak

B.Sc. (honours) McGill University, Montréal, Canada, 1998

A THESIS SUBMITTED IN PARTIAL FULFILLMENT OF

THE REQUIREMENTS FOR THE DEGREE OF

MASTER OF SCIENCE

in

THE FACULTY OF GRADUATE STUDIES

Department of

EARTH AND OCEAN SCIENCES

We accept this thesis as conforming

to the required standard

THE UNIVERSITY OF BRITISH COLUMBIA

May 2001

In presenting this thesis in partial fulfilment of the requirements for an advanced degree at the University of British Columbia, I agree that the Library shall make it freely available for reference and study. I further agree that permission for extensive copying of this thesis for scholarly purposes may be granted by the head of my department or by his or her representatives. It is understood that copying or publication of this thesis for financial gain shall not be allowed without my written permission.

Earth and Ocean Sciences
The University of British Columbia
2075 Wesbrook Place
Vancouver, Canada
V6T 1Z1

Date: May 23, 2001

Abstract

Submarine canyons are common bathymetric features that cut into the continental shelf from the continental slope. During upwelling favourable conditions over the continental shelf, submarine canyons display enhanced upwelling, heavily impacting shelf-slope mass exchange. In this thesis, laboratory experiments were conducted to quantify how velocity, stratification and rotation affect canyon upwelling.

Currents were forced by changing the rotation rate of an already rotating tank. Over time, the forced currents evolve, or spin-up, until the fluid within the tank is once again rotating at the same rate as the tank itself. A difference in the spin-up behaviour is observed when a canyon is not present in the laboratory topography. The dynamics that govern flow evolution when a canyon is not present are Ekman suction and diffusion, both of which can be affected by a sloped bottom boundary layer. A numerical model is developed that replicates the spin-up of a stratified fluid over the changing slopes of the laboratory topography in the absence of a canyon, incorporating both the decay of Ekman suction and the change in the diffusion of momentum which occur as the boundary layer flow is arrested by buoyancy effects.

Observed spin-up with a canyon present is compared to predicted spin-up without a canyon. The difference measures a force imposed by the canyon, which is found to be proportional to $U^{2.5}f^{0.5}/N$, where U is the shelfbreak velocity, f is the Coriolis frequency and N is the buoyancy frequency. This force relates to the flux of water crossing the shelfbreak through the canyon. The results are applied to Astoria canyon, suggesting that in a strong upwelling event, the flux of water through the canyon is $1.3 \times 10^5 \mathrm{m}^3\mathrm{s}^{-1}$, nearly 20 times larger than wind-induced upwelling over a similar length of the shelfbreak.

Table of Contents

List of Tables

List of Figures

Acknowledgements

I would like to give a heartfelt thank-you to my supervisor, Susan Allen. Her insight and enthusiasm have been a wonderful inspiration. I could not have hoped for a better supervisor. Rich Pawlowicz has been a tremendous help. From my many hours in the first row of his lectures, to the time in his office working on theoretical ideas and on to his suggestions on the text, his teachings and guidance have been superb. Noboru Yonemitsu gave tremendously useful and enthusiastic contributions to the developments in the laboratory. His selfless contribution of time and energy, his curious nature and his cycling advice have all been extremely helpful. David Jones and Doug Latornell kept the table turning in the laboratory.

Tawnya Peterson is personally responsible for the fact that my head is still firmly attached to my shoulders. I dedicate this project to my parents and sisters who have given me their care and support throughout my time in Vancouver.

Chapter 1

Introduction

Submarine canyons are bathymetric features that cut into the continental slope, often extending past the shelfbreak and incising the continental shelf. During upwelling favourable conditions, the upwelling signal is enhanced in these canyons. The upwelled water is rich in nutrients, and as a result canyons are regions of high biological productivity. Upwelling events last for several days. An upwelling episode contains an early transient phase and a longer lasting, steady advection phase. The transient phase is well described by linear dynamics (*Allen*, 1996) but the second phase is highly nonlinear and difficult to characterize. This thesis examines how the variation of current velocities, density stratification and Coriolis frequency control the amount of water that is upwelled through a submarine canyon.

1.1 Background

The mesoscale current field on the continental shelf is forced by winds, gravity and topography. Gravity is a body force while wind and topography are felt through the boundaries of the ocean. Aside from near seamounts and islands, the effects of wind and topography are combined only at or near the edges of the ocean basins in a region known as the continental margin. This margin is comprised of the continental shelf, the shelfbreak, the continental slope, and the continental rise (Figure 1.1).

The continental shelf extends seaward from the coast for a distance that varies from 3 km to 500 km. The edge of the continental shelf is marked by a sudden and considerable

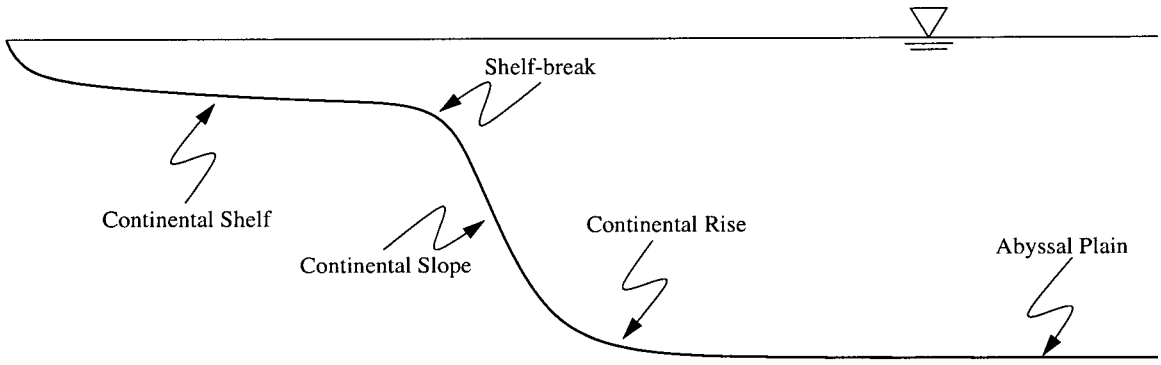

Figure 1.1: Cartoon of generic shelf topography described in the text. Submarine canyons cut into the continental slope

increase in the bottom slope. The location of this change in slope is known as the shelfbreak and is believed mark the edge of the sialic continental mass. The steep region downslope of the shelfbreak is the continental slope, where ocean depth increases quickly to over 1 km. The continental rise marks a decrease in the slope and connects the continental slope to the abyssal plains of the deep ocean.

To lowest order, the ocean is dominated by a geostrophic balance at low frequencies, which effectively implies that horizontal pressure gradients in the water column are balanced by the rotational influences of the planet. One of the effects of this balance on the coastal ocean is that currents generally follow isobaths. Due to the steepness of the continental slope, exchange across the shelfbreak is limited to secondary circulation. Areas of complex shelfbreak geometry, however, will have stronger cross-shelfbreak currents since geostrophic balances tend to break down in these regions. An example of such a feature is a submarine canyon.

Submarine canyons are common along ocean edges (Figure 1.2). They are conduits for sediment deposition to the deep ocean, and are often sites of genesis for turbidity currents.

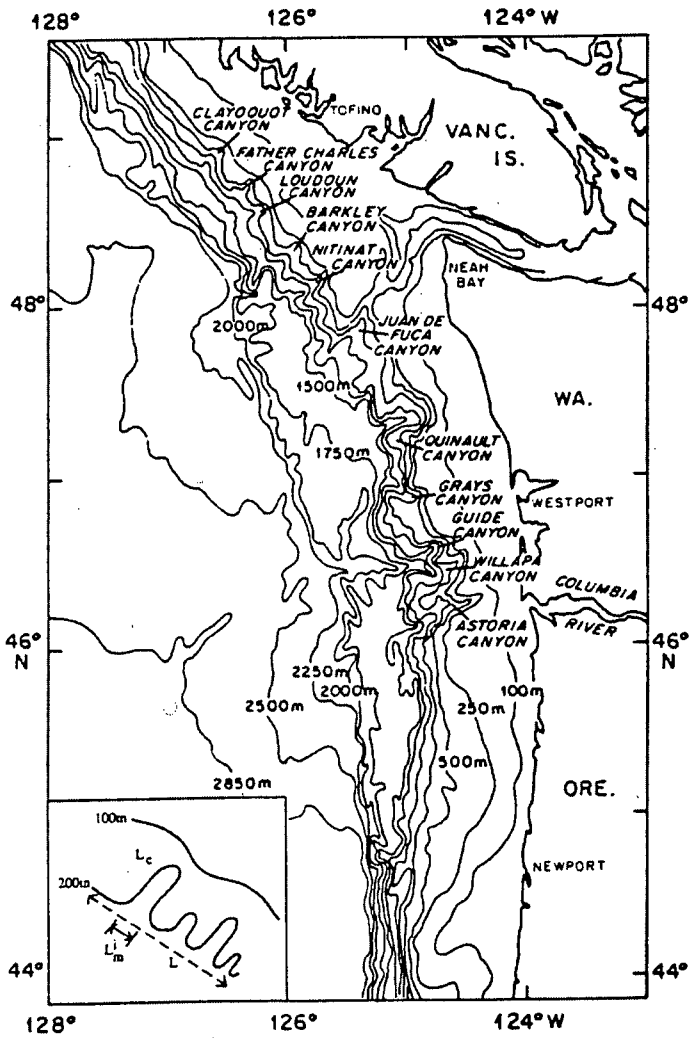

Figure 1.2: Submarine canyons of the west coast of North America. Reproduced with permission from *Hickey* 1995.

Submarine canyons are only present in areas where the slope is greater than 3° (*Thurman*, 1994) and are believed to be formed by erosional action of these turbidity currents. Where these features reach past the shelfbreak and cut into the continental shelf, they are sites of enhanced upwelling and downwelling onto and off of the continental shelf and as such are important in determining watermass distribution over the continental shelf and slope as well as mass exchange across the shelfbreak.

1.1.1 Flow Characteristics in and around Submarine Canyons

Flow patterns within a submarine canyon are driven by the geostrophic pressure gradient (*Freeland and Denman*, 1982). The interaction of the density stratified ocean with the steep and complex topography results in a strongly non-linear, baroclinic, three-dimensional flow-field (Figure 1.3), the details of which still remain unclear. In order for flow characteristics to be affected by topography, deviations from geostrophy within the canyon must be strong. Canyon effects are strong over more *narrow* canyons (those whose width is less than half of the Rossby deformation radius[1]; *Klinck*, 1988), although recent measurements over Barkley Canyon (*Vindeirinho*, 1998; see Figure 1.2) showed that upwelling effects can be measured even over wider canyons. It also seems that the width of a canyon and its radius of curvature where it meets the shelfbreak play an important role in the volume of upwelling through a canyon (*Allen and Hickey*, in prep.).

One of the best field datasets examining flow through a canyon was gathered over Astoria Canyon (*Hickey*, 1997), which cuts into the continental shelf west of the mouth to the Columbia River. Results of this field work demonstrated that while currents in the upper layers of the ocean (100 metres above the canyon-rim) are barely affected,

[1]The Rossby deformation radius is equal to $\sqrt{gD}/f$ where g is gravity, D is the depth and f is the Coriolis frequency.

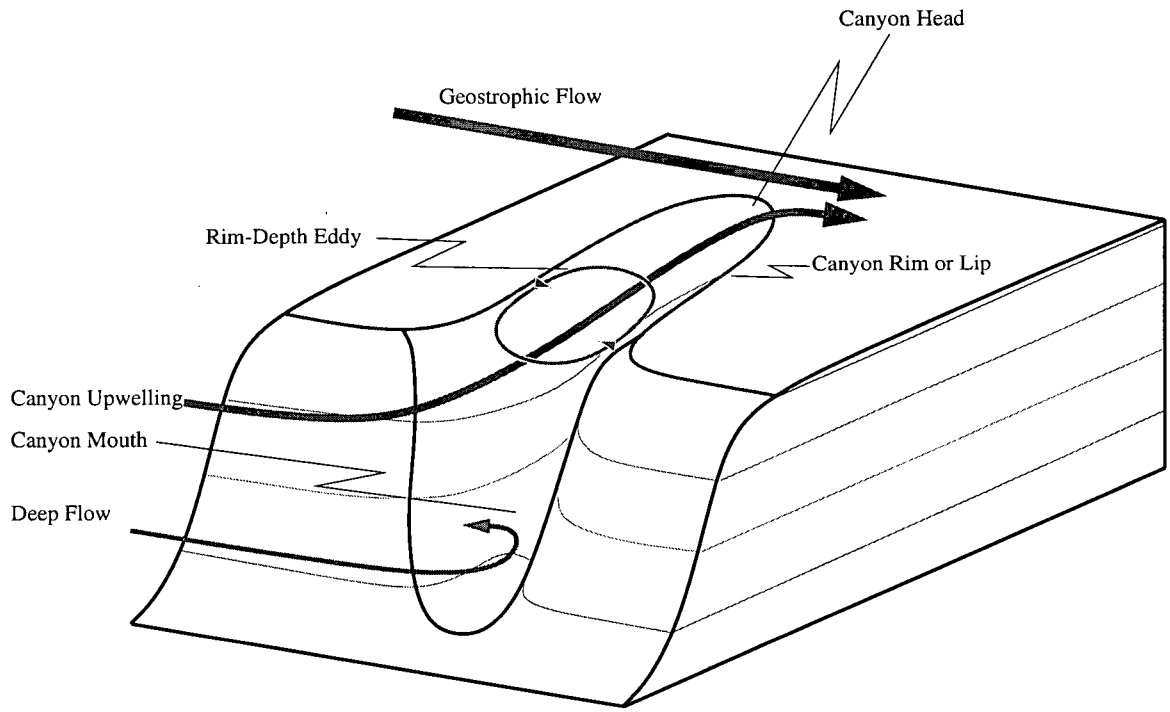

Figure 1.3: Schematic diagram showing the flow features in and around a submarine canyon.

if at all, by the presence of a canyon below, the water below this depth is stretched as it passes over the canyon rim (Figure 1.4). This stretching results in an addition of cyclonic vorticity to the flow field. Submarine canyons have an eddy at rim-depth (*Allen et al.*, submitted). Laboratory results suggest that barotropic controls of the rim-depth eddy include the strength of the velocity field (*Pérenne et al.*, 1997), while scaling arguments show that the shape of the canyon (triangular- versus square-shaped rim) is also important in baroclinic environments (*Allen and Hickey*,in prep.).

Geometry also affects the nature of the upwelling environment. Some canyons, such as Juan de Fuca canyon, cut far into the continental shelf. (In the case of Juan de Fuca Canyon, it cuts all the way into the shelf, eventually becoming Juan de Fuca Strait.)

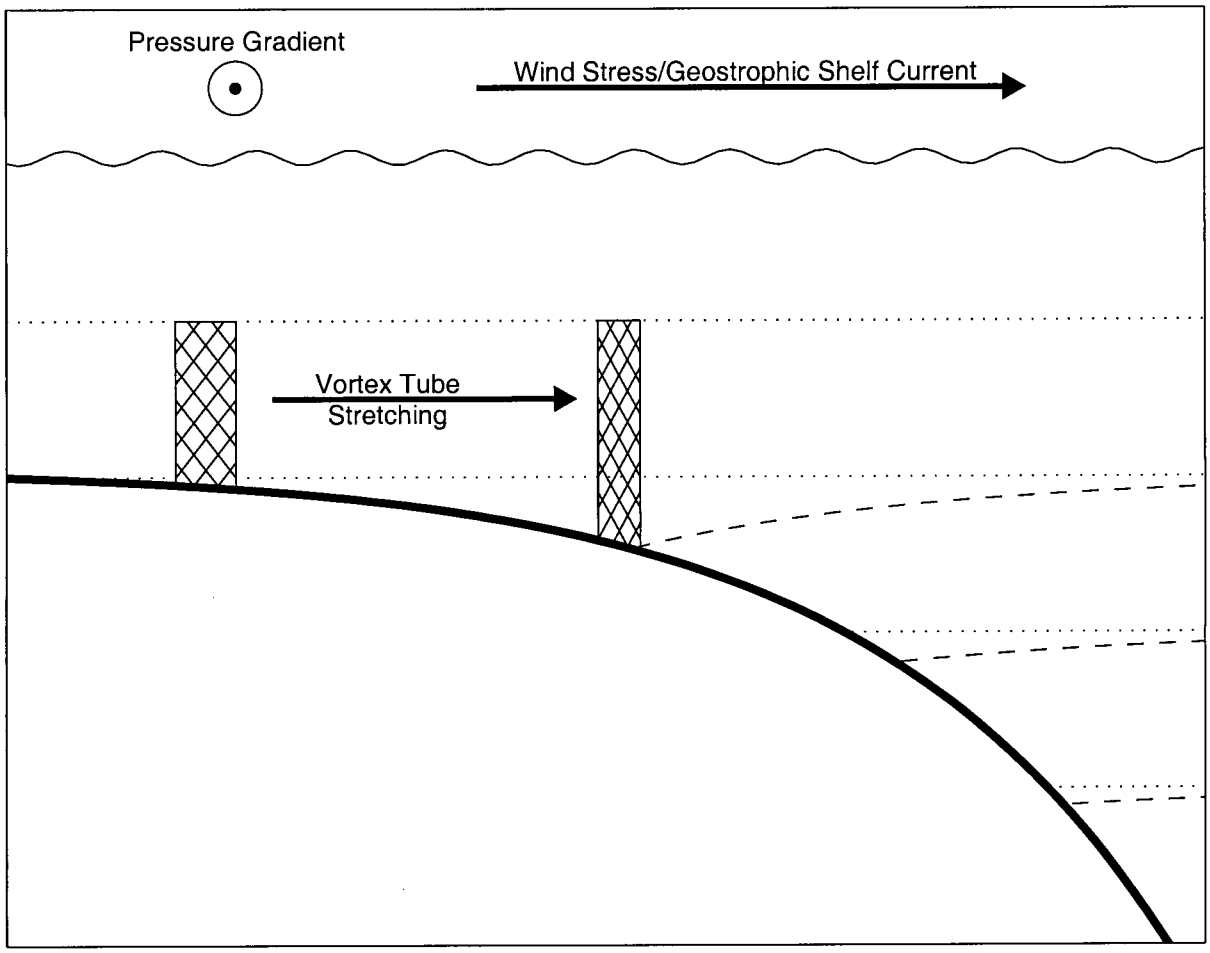

Figure 1.4: Vortex stretching experienced by a fluid as it travels over topography. The topography in this case is meant to be the upstream lip of a canyon. The cross-section is oriented such that you are looking towards shore. The wavy line represents the ocean surface. Lines of constant depth (dotted lines) and constant density (dashed lines) are also shown. Arrows are also present giving directions of prevailing winds and currents. The pressure gradient coming out of the page is representative of the northern hemisphere (i.e. it would be into the page in the southern hemisphere). The fluid column (box filled by diagonal cross-hatching) increases its vertical length as it travels over the steep topography, resulting in an addition of local vorticity to the flow field.

This canyon exhibits stronger, more consistent upwelling (*Allen*, 2000) while a tapered, more *normal* canyon such as Astoria Canyon exhibits pulses of upwelling (*Hickey*, 1997). *Normal* canyons appear to only become important when the along-shore currents are strong (*Allen*, pers. comm.; *Allen and Hickey*, in prep.; *Hickey*, 1997).

The Astoria dataset has been used to calibrate numerical models. These numerical models revealed that the advection of deep water onto the shelf was related to the canyon dimensions and stratification (*Klinck*, 1996) and that upwelling through a submarine canyon is an order of magnitude stronger than the on-shore flux at the shelfbreak in the absence of a canyon (*Allen*, 1996).

Submarine canyons not only affect vertical currents (upwelling and downwelling) but horizontal ones as well. Bottom currents downstream of the Hudson Shelf Valley (*Han et al.*, 1980) and Astoria canyon (*Hickey*, 1997) were observed to be in phase with flow variations within the canyon during upwelling-favourable conditions. In a downwelling-favourable scenario, (one where the currents on the shelf are travelling in the same direction as the shelf waves,) the flow patterns change. When downwelling currents travel past the Grand-Rhone Canyon in the Mediterranean Sea, the flow does not extend onto the shelf downstream (*Durrieu de Madron*, 1994).

Since upwelling takes place when the flow is travelling in the direction opposite to the propagation of shelf waves, a train of standing Rossby shelf waves forms downstream of the canyon. These waves do not form when the flow is downwelling favourable. The formation of these waves and their effect in a homogeneous fluid experiencing oscillatory forcing has been studied numerically and in the laboratory (*Pérenne et al.*, 1997). The standing waves impose a drag on the flow during upwelling events, but there is no equivalent set of waves formed during the downwelling phase of the oscillatory forcing. The unbalanced drag results in a rectified flow travelling in the downwelling-favourable direction along the shelf.

Tidal oscillatory forcing can result in a rectified flow travelling in the direction of shelf waves propagation over canyonous bathymetric regimes as may be inferred by the current regime near Grand-Rhone Canyon (*Durrieu de Madron*, 1994). Off the west coast of North America, however, the upwelling and downwelling patterns are seasonal, and while strong tidal oscillations are present (*Foreman and Thomson*, 1997), they do not affect the mean currents strongly enough to eliminate the upwelling fluxes during the summer months. It is therefore possible that, in this region of the world, standing waves remain present over the continental shelf during the summer months, while upwelling persists.

1.1.2 The Rossby Number

The degree to which rotation is important in a flow is expressed in a non-dimensional number known as the Rossby number. The Rossby number is defined as

$$R = \frac{U}{Lf} \tag{1.1}$$

where U is a characteristic velocity scale, L is a characteristic length scale and f is the Coriolis frequency, $f = 2\Omega \sin\alpha$, where Ω is the rotation rate of Earth and α is the latitude.

The Rossby number results from a scaling analysis of the momentum equation,

$$\frac{\partial \vec{u}}{\partial t} + \overbrace{\vec{u}\nabla \cdot \vec{u}}^{\text{advection}} + \overbrace{f\hat{k} \times \vec{u}}^{\text{rotation}} = \sum Forces, \tag{1.2}$$

where $\vec{u}$ is the velocity and k is the unit vector in the vertical direction. When examining ocean currents at low frequency, it can be assumed that $\partial\vec{u}/\partial t$ is small. This leaves only the advection and rotation terms, which are labeled above, on the left hand side of the equation. By scaling (1.2) with appropriate length and velocity scales, L and U, respectively, the ratio of the two terms above will be the Rossby number. When $R \ll 1$,

a reasonable assumption is that advective terms are unimportant and the geostrophic balance will govern flow behaviour.

1.1.3 Upwelling and Submarine Canyons

Currents on the continental shelf are governed by geostrophy to lowest order. (A flow velocity of 10^{-1} m·s^{-1}, a Coriolis frequency of 10^{-4}s^{-1}, and a lengthscale of 10^{5}m, the Rossby number is 10^{-2}, indicating that rotation is far more important than advection for these currents.) Along the shelfbreak a front is present that marks the shelf-slope interface and is an effect of the geostrophic balance. Upwelling currents are generated primarily as a secondary current caused by the divergence in surface currents away from the coast due to the southward wind stress (Figure 1.5). Off the west coast of North America, winds blowing to the south result in westward transport in the upper Ekman layer. By continuity, the depleted water at the coast is replaced from below, resulting in upwelling. The wind-driven offshore transport also creates an offshore pressure gradient, resulting in a southward flow over the continental shelf. Southward currents in this region of the world are typical in the summer upwelling season.

When this southward travelling current encounters a submarine canyon, due to the curvature of canyon bathymetry (typically less than or on the order of 10 km), geostrophy begins to break down. Advective terms increase and the current directions deviate from the regional isobaths. The region of continental shelf extending along the west coast of British Columbia, Canada and Washington, USA is cut by numerous submarine canyons (Figure 1.2). In upwelling-favourable scenarios, nutrient-rich water (*Freeland and Denman*, 1982) is advected onto the continental slope across the entire shelfbreak, with enhanced advection present in canyons (*Hickey*, 1997; *Allen*, 1996; *Klinck*, 1996) resulting in enhanced primary productivity in these regions (*Allen et al.*, 2001; *Vindeirinho*, 1998; *Mackas et al.*, 1997). Analysis of chemical properties suggests that the waters

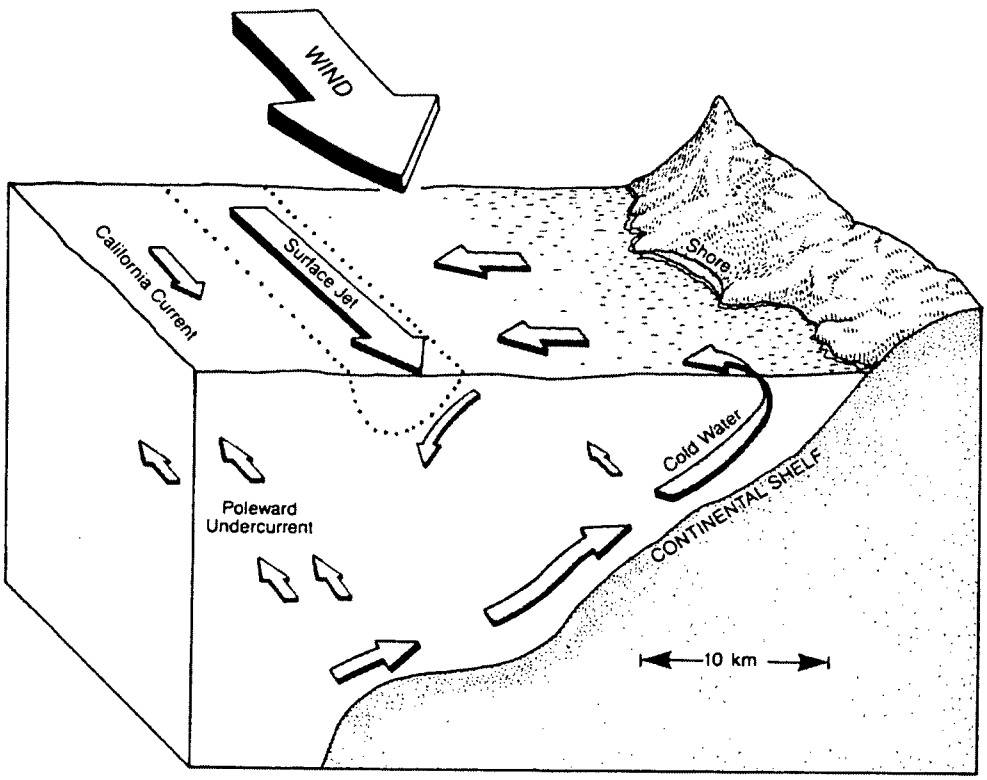

Figure 1.5: Wind-driven coastal upwelling as described in the text. Reproduced with permission from *Thomson* (1981).

being upwelled through Juan de Fuca canyon have a source depth of 400 m (*Freeland and Denman*, 1982), although the geometry of Juan de Fuca canyon makes it a special case (*Allen*, 2000) . Scaling analysis predicts source waters for upwelling in other canyons to come from a depth of about 300 m (*Allen and Hickey*, in prep.).

Throughout most of the coastal ocean, primary productivity is dependent primarily on nutrients[2]. Nutrient levels in the ocean peak at approximately 500 m depth, tapering to a near-zero level at the surface. One of the sources of nutrients into the surface waters is upwelling, which brings deep, cold, nutrient-rich water to the euphotic zone. Downwelling results in the opposite, arresting fertilization of surface waters from below. Upwelling and downwelling can be forced by wind-driven currents and by topographically-driven currents. Topographically forced upwelling is strong over the continental shelf and is one of the principle reasons for high biological productivity in coastal regions around the world.

1.1.4 Modeling of Canyon Flow in the Laboratory

Due to the steep nature of canyon topography and the baroclinic controls on the three-dimensional flow field associated with these features, the flow in and around submarine canyons is complex. In addition to field studies (*Hickey et al.*, 1986; *Hickey*, 1997), analytical models (*Chen and Allen*, 1996) and numerical models (*Allen*, 1996;*Klinck*, 1996; *Klinck*, 1989), laboratory experiments (*Allen et al.*, in prep; *Boyer and Davies* 2000; *Pérenne et al.*, 1997) have been used to realize flow around submarine canyons. Due to the limitations of laboratory scaling, however, the flow field produced in the laboratory is similar but not identical to oceanographic flows (*Allen et al.*, submitted). Field observations over canyons give sparse data that are both costly and challenging to collect. As a result, advancements in understanding of currents in these regions relies

[2]Regions of the coast are, at times, limited by the micronutrient iron (*Hutchins and Bruland*, 1998)

heavily on both laboratory and numerical predictions.

Developing a better understanding of flow through submarine canyons has been difficult due to the nonlinear nature of the flow and the steep topography of these features. Comparisons between laboratory and numerical model outputs have revealed that the two do not give identical results (*Allen et al.*, in prep.). While laboratory models can be expected to truthfully obey the physics of a problem, quantifying the results is not always possible. Numerical models, on the other hand, have the opposite relation. The results that they give can be easily quantified, but some of the physics must be removed. In this study the goal has been to develop a method of quantifiably measuring the upwelling in a submarine canyon with a laboratory model.

1.2 Method of Solution

The laboratory experiments performed here as well as those studying canyons in the past (*Allen et al.*, submitted; *Pérenne et al.*, 1997) are performed in a cylindrical rotating tank where velocities in the tank are forced by altering the rotation rate. In order to create an upwelling favourable environment, the rotation rate of the tank is increased (causing the currents in the tank to travel in the direction opposite to shelf waves). Quantifying the upwelling flux directly is extremely challenging if not impossible. In this thesis, the upwelling flux through the canyon is measured by examining how the surface currents of the tank evolve.

1.2.1 The Effects of Rotation and a Canyon on Flow Evolution

A non-rotating current travelling over a flat bottom boundary will have a governing equation of

$$\frac{D\vec{u}}{Dt} = \nu\nabla^2\vec{u}, \tag{1.3}$$

where $\vec{u}$ is the velocity and ν is the kinematic viscosity. Given a no-slip boundary condition along the bottom boundary, the timescale for velocity evolution is $H^2\nu^{-1}$, where H is the fluid depth. For a fluid that is 0.1 m deep and has a kinematic viscosity of 10^{-6} m^2s^{-1}, this timescale is 10^4 seconds, (or a little over 2 and a half hours).

In this problem, however, the currents are rotating and the forcing mechanism itself is dependent on increasing the rotation rate. A byproduct of this forcing is the addition of anticyclonic vorticity to the flow field. As a result, an Ekman layer will form along the bottom boundary, which will advect the water radially outwards. This process causes vortex stretching in the interior, which will accelerate the flow evolution. Analysis of the boundary layer response to the induced current makes possible predictions of how the boundary layer will cause the interior flow to evolve, or spin-up. For a flat-bottom tank, the timescale for flow evolution is $H\Omega^{-1/2}\nu^{-1/2}$ (*Greenspan*, 1968). For a rotation rate of 0.25 s^{-1}, and the same depth and viscosity as above, this will result in a timescale of 200 seconds.

In this study, the model topography replicates the continental shelf and slope. The evolution of currents are observed in the presence and absence of a canyon. Experiments show that the timescale of flow evolution with a canyon present is significantly less than for the canyon-free scenario. Differences in flow evolution can be used to quantifiably measure the force imposed by the canyon on the flow. This force, F, which is used to determine the upwelling through a canyon, is defined as

$$F = \rho C_d L_1 L_2 U^2, \tag{1.4}$$

where ρ is the density, C_d is a drag constant, L_1 and L_2 are appropriate lengthscales, and U is the velocity. The appropriate lengthscales for this problem are not examined in this thesis, although suggestions by *Allen and Hickey* (in prep.) suggest that they are the width of the canyon at the shelfbreak and the radius of curvature of the shelfbreak

as it turns into the upstream flank of the canyon. It is believed that C_d is dependent on the velocity, stratification and rotation rate of the flow approaching the canyon as well as canyon geometry. Although effects of geometry are not studied here, the exact relationship between C_d and the other properties is examined in this thesis.

1.2.2 Organization of This Thesis

Chapter 2 will discuss work done in the laboratory. The choice of scales used in the model, the laboratory methods performed for data collection and velocity measurement, and an error analysis are presented. Chapter 3 examines the spin-up behaviour in the absence of a canyon. It begins by giving a brief history of the spin-up problem and introduces the limitations of pre-existing theory to the this study. Extensions of current theory are developed and tested against laboratory data. Chapter 4 examines the spin-up problem when a canyon is introduced to the model. The effects of a canyon are measured and the forces imposed by the canyon in the various trials are determined. Analysis finds a relationship between the force and the flow properties. The thesis closes with a discussion of results and conclusions in Chapter 5.

Chapter 2

Laboratory Methods and Data Analysis Techniques

The goal of laboratory modeling, also known as physical modeling, is to better understand a phenomenon found in nature by replicating it in a controlled laboratory setting. Quite often one is not able to reproduce the field scenario exactly, and the important non-dimensional quantities are matched by scaling the appropriate dimensional quantities instead. Clearly, the flow patterns being modeled in this study must be scaled, as those in the ocean have lengthscales that are O(km). The tank used for these experiments is one meter in diameter and the topography within mimics that of a generic coastal ocean, albeit at a 10-fold vertical exaggeration: an abyssal plain in the tank centre adjoins the continental slope, leading to a continental shelf and ending in a coastline at the tank edge (recall Figure 1.1). The vertical scaling is necessary in order to correctly replicate viscous effects in the laboratory. To study the effects of a submarine canyon, a 22° slice of the continental slope is removed and replaced by a topographic section that mimics the bathymetry of a submarine canyon (Figure 2.1). For some experiments, the topography was radially symmetric, i.e. there was no canyon present in the laboratory set-up.

2.1 Scaling Analysis

The non-dimensional parameters that are important to this problem are the Ekman number, the Rossby and the Burger number. The Ekman number, Ek, is the ratio of the bottom boundary layer thickness, δ, to the water depth. Following *Hewett* (1998),

the chosen depth scale was the shelfbreak depth, H_s, giving an Ekman number of

$$Ek = \frac{\delta}{H_s}. \tag{2.1}$$

The Rossby number, Ro, relates the importance of advection to rotation

$$Ro = \frac{U}{f\mathcal{R}}, \tag{2.2}$$

where U is the velocity, $\mathcal{R}$ is the radius of curvature of the upstream flank of the canyon and f is the Coriolis frequency. The Burger number, Br, relates the importance of buoyancy to rotation and is equal to

$$Br = \frac{NH_s}{fL_c}, \tag{2.3}$$

where H_s is the shelfbreak depth, L_c is the length of the canyon normal to the shelfbreak from its head to its mouth, N is the Brunt-Väisälä frequency or buoyancy frequency,

$$N = \sqrt{-\frac{g}{\rho_o}\frac{\partial \rho}{\partial z}}, \tag{2.4}$$

g is gravity ρ_o is a reference density, ρ is the density and z is the vertical direction. It was discovered during analysis that the Froude number is also important. The Froude number, Fr, is defined as

$$Fr = \frac{U}{NH_s} \tag{2.5}$$

and gives the relative importance of velocity to buoyancy effects. The laboratory model was originally designed to mimic Astoria canyon (Figure 2.2), and the laboratory scaling is therefore matched to the oceanographic conditions found there (Table 2.1).

The values $N = 2.2\text{s}^{-1}$, $f = 0.52\text{s}^{-1}$ and $U = 1.16\text{cm s}^{-1}$ were taken as a set of *standard* values. To see how these values affect the flow, they were changed separately in order to better determine how the parameters affect flow evolution. The trials performed are shown in Table 2.2.

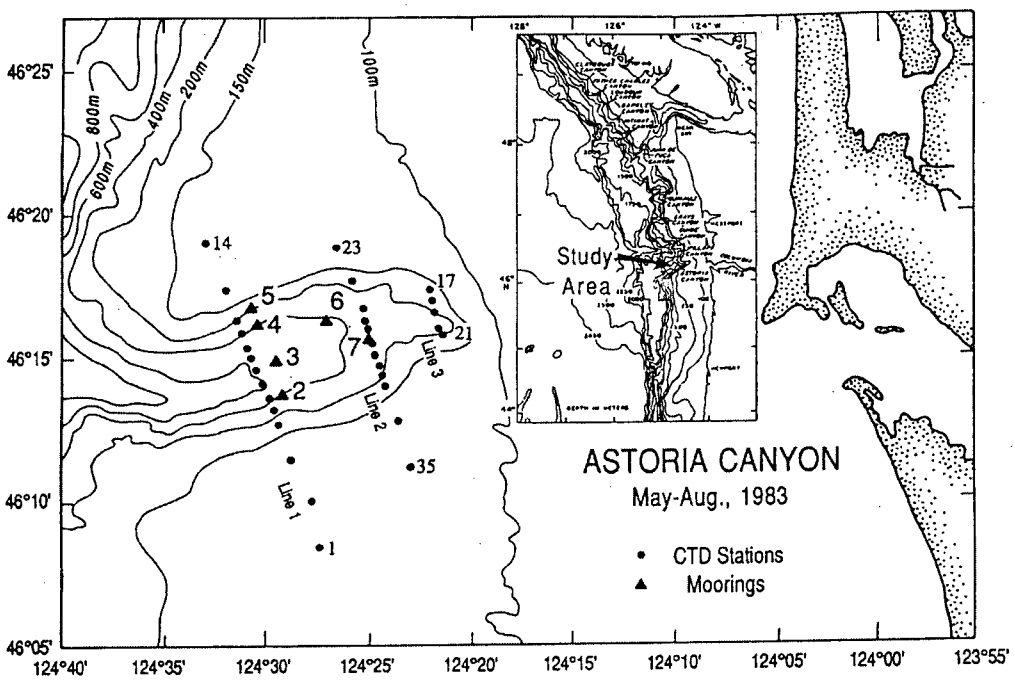

Figure 2.2: Bathymetry of Astoria canyon. Reproduced with permission from *Hickey* (1997)

Parameter	Astoria	Lab
L_c	22 km†	8 cm
H_s	150 m†	2 cm
$\mathcal{R}$	4.5 km†	4 cm
δ	50 m‡	2 mm
N	10^{-2} s$^{-1\dagger}$	2 s^{-1}
f	10^{-4}s^{-1}	0.5 s^{-1}
U	20 cm s^{-1}	1.2 cm s^{-1}
R	0.44	0.60
Ek	0.3	0.1
Bu	0.13	0.3
Fr	0.13	0.25

Table 2.1: Scaling of parameters used in laboratory modelling. The blank line marks a separation between dimensional and non-dimensional values † denotes values are from *Allen and Hickey* (in prep.); ‡ denotes values are from *Hewett* (1998)

Trial	N_{SB}	f	Δf
1	2.2	0.52	0.12
2†	**0.0**	0.52	0.12
3*	**1.1**	0.52	0.12
4	**4.4**	0.52	0.12
5	2.2	**0.40**	0.12
6	2.2	**0.70**	0.12
7	2.2	0.52	**0.09**
8	2.2	0.52	**0.06**

Table 2.2: Trials performed in the laboratory. Each trial was performed with and without a canyon present in the tank topography. $U_{SB} = r_{SB}\Delta f$ is equal to the initial geostrophic current at the shelf-break, where r_{SB} is the radial location of the shelf-break in the tank. Units for each of the dimensional parameters are $N_{SB} = [\text{s}^{-1}]$, $f = [\text{s}^{-1}]$, $\Delta f = [\text{s}^{-1}]$ and $U_{SB} = [\text{m}\cdot\text{s}^{-1}]$. Values of N_{SB}, f and Δf that have been changed from the *standard* values are accented in bold. † Trial 2 uses a homogeneous fluid; * Results for trial 3 were lost and could not be analyzed.

2.2 Experimental Trials

In order to avoid mixing and to achieve solid body rotation more quickly, the tank was filled with stratified water while rotating over a period of approximately 90 minutes, and was left to spin-up for an additional two hours, ensuring that it had achieved solid-body rotation. Stratification was achieved by adding salt, hence density diffusion is assumed negligible over the course of an experiment. Stratification was created using the Osler method (*Osler*, 1965), where two containers are filled with equal volumes of fresh and salt water, respectively. These containers are connected at the bottom by a piece of tubing, and there is a mixer in the salt water container. Another piece of tubing attaches the container housing the saline water to the tank. If the Olser method is used to fill a tank containing only vertical walls, then it will result in a linear stratification. Due to the sloping nature of the topography in our tank, however, the stratification is stronger near the surface (Figure 2.3).

Velocity forcing in the tank was achieved by varying the rotation rate of the tank, which was accelerated from an initial rotation rate to a final rotation rate over one rotation period of the tank. This impulse is sufficiently long to allow development of an Ekman layer along the bottom, but short enough to leave the interior rotating at approximately its original rate. Pliolite VT-L particles were used as tracers and were placed on the fluid surface. (These particles are produced by Goodyear Chemical Company.) In order to reduce surface tension, the water which was used to fill the tank was treated with small amounts of dish soap and Photo-Flo (produced by Kodak). A videocamera mounted in the rotating reference frame recorded the flow and velocities were calculated using MatPIV, a particle image velocimetry (PIV) package for Matlab (*Sveen*, 2000). This technique provides a continuous time-series of velocity data, allowing us to observe the evolution of the flow field at the tank surface. Pathlines were created by overlaying

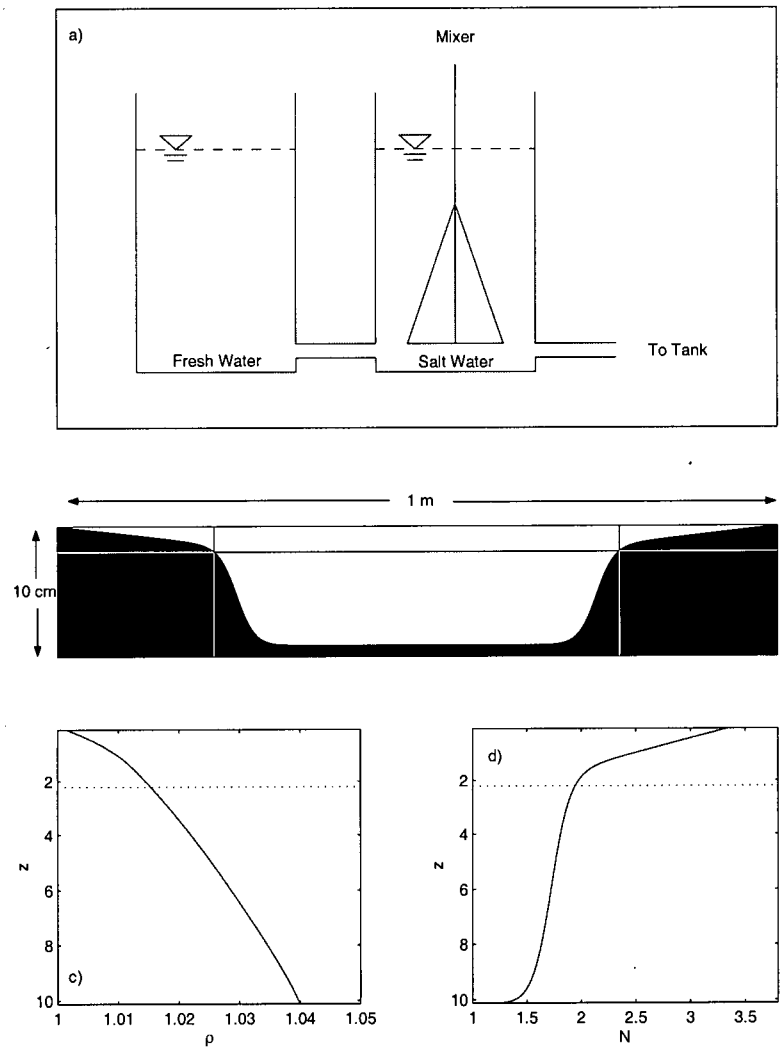

Figure 2.3: Creation of a density gradient in the laboratory a) Schematic showing method for creating a density stratified fluid to fill the tank. b) Cross-sectional view of the tank bathymetry. The location of the shelfbreak is highlighted by the cross-hairs. The tank was filled from bottom to top, with the stratified water coming from the buckets shown in a). This results in the density profile shown in c) and the buoyancy frequency, N, shown in d). Values shown in c) and d) are theoretical expectations giving a stratification representative of Trials 1, 7 and 8. The dotted line represents the location of the shelfbreak

images from the video camera, providing a tool for qualitative flow visualization.

2.3 PIV techniques

PIV is a very powerful correlation tool for flow-field analysis as it does not suffer from complications arising from tracking individual particles. PIV traces particle distributions in a flow field, rather than the particles themselves. The fundamental concept behind this method is that a digital image can be considered as a signal field analagous to a digital time-series. In order to obtain velocity measurements, two sequential images are subsampled in small regions known as "interrogation windows", and the displacement of particles between two video frames within a given interrogation window is determined by cross-correlation methods (Figure 2.4). The cross-correlation function, Cr, is defined as

$$Cr(x,y) = \sum_{i=-M/2}^{M/2} \sum_{j=-N/2}^{N/2} Im_1(i,j) Im_2(i+x, j+y) \tag{2.6}$$

where Im_1 and Im_2 are the interrogation windows being compared and, usually $N = M$. Calculating Cr using the method in (2.6) will require $O(N^4)$ computations. This number can be reduced by applying the correlation theorem: correlation in the spatial domain is equivalent to multiplication in the frequency domain. This theorem allows (2.6) to be rewritten as

$$Cr = \Re\{\text{ifft}\,[\text{fft}(Im_1) \cdot \text{fft}(Im_2)^{*r}]\} \tag{2.7}$$

where fft is the Fast Fourier Transform, ifft is the Inverse Fast Fourier Transform and I^{*r} is the reverse conjugate matrix of I. (For a matrix $A_{m\times n}$,

$$A^{*r} = \begin{bmatrix} a^*_{m,n} & a^*_{m-1,n} & \cdots & a^*_{1,n} \\ a^*_{m,n-1} & a^*_{m-1,n-1} & \cdots & a^*_{1,n-1} \\ \vdots & \vdots & \ddots & \vdots \\ a^*_{m,n} & a^*_{m-1,n} & \cdots & a^*_{1,n} \end{bmatrix}, \tag{2.8}$$

where the * denotes the complex conjugate.) Using this method decreases the computational expense from $O(N^4)$ to $O(N^2 \log N)$ computations.

If there is a correlation between the two images, this will be expressed by a noticeable peak in the function Cr. The position of this peak relative to the center of the first interrogation window gives the displacement between the two images. It is assumed that the particle displacement between two frames is homogeneous within a given interrogation window.

2.3.1 Error Analysis and Propagation

A balance between efficiency of experimental procedures and minimization of error must be found. The accuracy of measurements attained by PIV techniques is a combination of several aspects in the procedure beginning with recording techniques and ending with evaluation methods. In order to determine the error in PIV measurements, *Raffel et al.* (1998) create an artificial set of images with known particle displacements numerically. They then analyze the artificial images using PIV in order to empirically determine the error in measurements. This section presents a breakdown of their findings, as relevant to this study.

- Particle Image Diameter (ϵ_{ID})

  Raffel et al. (1998) show that for cross-correlation between two images, particle sizes slightly larger than 2 pixels is ideal. For the window size and resolution used in the experiments, an ideal particle size would be approximately 1.5 mm. While pliolite particles are definitely smaller than this, they have a tendency to coagulate. Examination of sections of three random images suggests that the average particle size is near 4 pixels in diameter (Fig. 2.5). The interrogation windows used were 32x32, giving the random error due to particle image diameter as approximately

0.015 pixels.

A bias error can be introduced when particles are small. Sub-pixel locations are determined using a three-point estimator. For particles smaller than one pixel, this bias can be significant although this error quickly diminishes for larger particles. For particles greater than two pixels, the error is less than $O(0.001$ px) and can be ignored.

- Particle Image Shift (ϵ_{IS})

  PIV uses the Fourier transform which inherently assumes that windows are periodic. If displacements are larger than half the window size, aliasing will occur. Introducing a displacement between the two interrogation windows improves accuracy of PIV measurements. A shift was assumed to compensate for average velocities in the tank (0.5 cm·s^{-1}), but this will still allow errors in velocity calculations. Velocities in the tank during PIV evaluations had a maximum value of 1.8 cm·s^{-1}. This is equal to less than 4.5 pixels per frame. For a Particle Image Diameter of 4 pixels, and a 32x32 interrogation window, a random error of 0.05 pixels is predicted. By shifting the second interrogation window, this error is reduced to 0.045 pixels. Late in time, when velocities are near zero, the shift described above gives a predicted error of 0.04 pixels. It will be assumed hereafter that the error is consistently 0.045 pixels.

- Image Quantization (ϵ_{QL})

  Video data were stored in 8-bit resolution. *Willert* (1996) and *Raffel et al.* (1998) both found that increasing quantization levels has very little effect on the uncertainty of measurements. In fact, decreasing the quantization levels from 8 bits per

pixel down to 4 has practically no influence on the anticipated error. For a particle density of 10.2 particles in a 32x32 interrogation window, which is significantly lower than the values from these experiments, the uncertainty is expected to be 0.025 pixels.

- Background Noise

  For image quantization of 4 bits per pixel or greater, RMS-error is essentially unaffected by noise (*Raffel et al.*, 1998).

- Displacement Gradients (ϵ_{DG})

  Experimental results show that the steepest gradients in displacement will occur across the shelf-break late in experiments with strong stratification. Displacement gradients in these trials are found to have a maximum value of 0.07 (pixels per pixel). *Raffel et al.* (1998) find that for experiments similar to the ones presented here, this will result in an uncertainty of 0.15 pixels.

It is crucial to note that all estimates for error above err on the side of caution; the error predicted above is representative of the flow field at its most troublesome velocities. The total error in calculations can be expected to be:

$$\begin{aligned} \epsilon_{tot} &= \sqrt{\epsilon_{ID}^2 + \epsilon_{IS}^2 + \epsilon_{QL}^2 + \epsilon_{DG}^2} \\ &\approx \sqrt{0.015^2 + 0.045^2 + 0.025^2 + 0.15^2}\text{px} \\ &\approx 0.16\text{px} \end{aligned} \tag{2.9}$$

Clearly, ϵ_{DG} dominates the RMS error over the shelf-break and continental slope. Over the continental shelf, $\epsilon_{DG} \approx 0.08$ px, which results in $\epsilon_{tot} \approx 0.10$ px. This leads to velocity uncertainties of about 5.6 mm·s^{-1} on the continental slope and 3.5 m.m·s^{-1} over the continental shelf.

Chapter 3

Laboratory Spin-up Without a Canyon

This thesis examines subtle differences in flow evolution with and without a submarine canyon present in the laboratory topography to determine quantitative expectations of the upwelling behaviour of water passing through a submarine canyon. Understanding the governing mechanisms that describe flow evolution in the tank without a canyon is critical in being able to measure the effect of a canyon on the evolution of the flow. The flow in the laboratory is forced by increasing the rotation rate of the tank. The process by which the flow evolves, which ends when the fluid is uniformly rotating at the increased rotation rate of the tank, is called *spin-up*. An example of the spin-up process in the laboratory is shown in Figure 3.1. This chapter develops the necessary theory to be able to successfully the predict spin-up processes when no canyon is present in the laboratory topography.

3.1 Introduction to the Spin-up Problem

The upwelling problem described in Chapter 1 and the spin-up problem are very similar in nature as they both describe a system in which ageostrophic events create a secondary current that strongly affects an otherwise geostrophic flow. In the classic spin-up experiment, a cylindrical, rigid-walled tank containing a viscous fluid in solid body rotation has its angular velocity increased impulsively by a small amount. Initially the fluid interior, which is away from any boundaries, is unaffected. Any walls not parallel to the axis of rotation, however, will develop Ekman boundary layers. In these layers, the

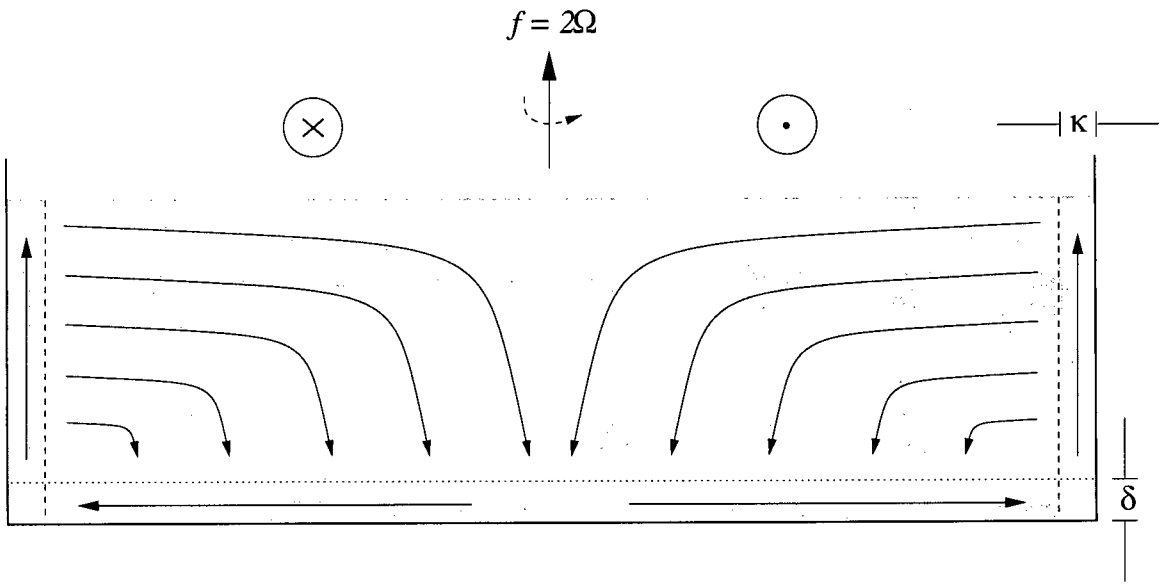

Figure 3.2: Cartoon showing the secondary circulation of a homogeneous fluid in a cylinder. The three-sided box (thick line) represents a vertical cross-section through a cylindrical tank holding water. The lowest order circulation of the flow, indicated by the vectors above the water, is anticyclonic, causing a divergence in the bottom Ekman layer (δ, below the dotted line). The Ekman divergence flow is fed by Ekman suction out of the interior, which adds cyclonic vorticity to the interior through vortex tube stretching. Water exits the Ekman layer at the tank edge where it enters the side-wall boundary layers (κ, outside the dashed lines). The side boundaries act as a replenishing source for water within the interior, which has a weak, radially inward flow.

was used to explain the rapid spin-up of rotating flows both theoretically and in the laboratory (*Greenspan and Howard*, 1963; *Greenspan*, 1964; *Greenspan*, 1965; *Greenspan*, 1968).

Other works went on to examine spin-up and spin-down in a homogeneous fluid where the Rossby number varied from -1 to 1 (e.g. *Wedemeyer*, 1964; *Benton*, 1973). These works were mathematical models, in that the flow was laminar and did not include instabilities characteristic of large Rossby numbers. The spin-up behaviour for larger

Rossby numbers is more complicated and hindered the development of a more general theory until more recently when more complex mathematical models (*O'Donnell and Linden*, 1991) were developed and non-linearities were further examined (*Konijnenberg et al.*, 1995). Other studies (e.g. *Linden and van Heijst*, 1984; *Konijnenberg et al.*, 1996) have looked at spin-up in non-axisymmetric containers, but the question of how variable topography - axisymmetric or non - might affect spin-up has received little attention.

3.1.1 The Spin-up of a Homogeneous Fluid Over a Flat Bottom

In homogeneous fluids, spin-up proceeds as described above (Figure 3.2). *Greenspan* (1963; 1968) examined the classic spin-up problem for cases where the increase in rotation rate, $\Delta\Omega$, is considerably less than the initial rotation rate, Ω, i.e. $\Delta\Omega/\Omega \ll 1$. A homogeneous fluid contained by a circularly cylindrical, flat-bottomed container has three important parameters that will determine its spin-up rate: a temporal Rossby number, $Ro_t = \Delta\Omega/\Omega$, which gives the ratio of the change in angular velocity to the final rate of rotation; a Froude number, $F = 4\Omega^2 R^2/(gH)$, where R is the radius of the tank, g is the gravitational acceleration, and H is the depth of the tank[1], which measures the relative importance of rotation to gravity; and an Ekman number, $E = \nu/(\Omega H^2)$, where ν is the liquid's kinematic viscosity, which represents the importance of viscosity to rotation (*Greenspan*, 1968). The spin-up of a fluid with a velocity described by $u_\phi(r) = \Delta\Omega r$, where $\Delta\Omega \ll \Omega$, will obey

$$u_\phi = \Delta\Omega r \exp(-t/\tau), \tag{3.1}$$

where u_ϕ is the tangential velocity, r is the radial coordinate and τ is a decay timescale equal to $1/(\Omega E^{-\frac{1}{2}})$.

Adding a non-homogeneous fluid or a more complicated tank shape causes the spin-up

[1]This is a curious definition for the Froude number as it seems to resemble the Burger number. It would make more sense for it to be defined either as the Burger number or as $4\Delta\Omega^2 R^2/(gH)$.

problem to become considerably more complex.

3.1.2 The Spin-up of a Stratified Fluids Over a Flat Bottom

Convection-style spin-up fails for non-homogeneous fluids as vertical motions are weakened, and eventually decay, due to the vertical structure of the fluid. In the late 1960's and early 1970's this problem began to receive much attention (*Benton and Clark*, 1974). In addition to the temporal Rossby number, the Ekman number and the Froude number, the Prandtl number and the Burger number become important parameters for stratified spin-up. The Prandtl number measures the relative importance of the diffusion of momentum against the diffusion of density and is defined as $P = \nu/\chi$, where ν is the kinematic viscosity and χ is the density diffusivity. The Burger number, $S = (N/f)^2$, where N is the buoyancy frequency,

$$N = \sqrt{-\frac{g}{\rho}\frac{\partial \rho}{\partial z}},$$

ρ is density, z is the vertical coordinate, and f is the Coriolis parameter, measures the relative importance of rotational and gravitational effects on the fluid. Laboratory spin-up experiments of a thermally-stratified fluid in a cylinder showed that Ekman layers of thickness $O(E^{1/2})$ still formed, but that Ekman-type effects die out before solid-body rotation is achieved, leaving the fluid in a quasi-steady state with the following characteristics (*Holton*, 1965):

- close to the horizontal boundaries, the interior rotates at the same rate as the tank that contains it;
- the angular velocity increases on a vertical length scale $L/S^{1/2} \gg \delta$, where L is the horizontal lengthscale of the tank and δ is the Ekman layer depth.

As there is no viscous stress within the Ekman layer, no Ekman pumping occurs and convection-like spin-up is halted, leaving diffusion of momentum as the mechanism for restoring solid-body rotation.

Further mathematical examination of the problem brought the relevance of these results into question. The result presented by *Holton* (1965) was determined with non-insulating side-boundaries. For an insulated fluid, buoyancy forces result in side walls being unable to accept the mass flux out of the Ekman layer due to gravitational effects of the accumulation of dense water along bottom edge of the tank (*Pedlosky*, 1967). *Pedlosky* (1967) concluded that as a result, spin-up by non-diffusive means would be halted prematurely and that the quasi-steady solution could not be achieved. These conclusions turned out to be incorrect. Despite this behaviour by the side walls, a secondary circulation does form (*Sakurai*, 1969; *Walin*, 1969) and the time required for the realization of the quasi-steady state described by *Holton* (1965) is $O(L/(\Omega\nu S)^{1/2})$ (*Walin*, 1969).

3.1.3 Sloping Ekman Layers

Ekman layers on a shallow slope have also received considerable attention in the more recent past, mostly driven by the desire to better understand mixing processes invoked by the bottom boundary layer of the ocean. The behaviour of an Ekman boundary on a slope in a homogeneous fluid generates the familiar Ekman spiral (*Pedlosky*, 1987). The addition of stratification to flow over a slope makes the problem considerably more difficult. Initial attempts to solve the problem specified density at the boundary (*Holton*, 1967; *Hsueh*, 1969), something that is more appropriate for atmospheric flows. Follow-up studies provided an insulated boundary (*Weatherly and Marin*, 1978; *Thorpe*, 1987) but the solutions gave curious results. For example, infinite transport was predicted for flat slopes.

When the problem was adjusted and solved for an oceanographically relevant case,

results showed that Ekman transport upslope causes the advection of dense water into a region of less dense water, imposing a downslope gravitational force on the fluid. Eventually the gravitational force is as strong as the rotational forces and the boundary layer arrives in a thermal-wind balance such that there is no cross-slope transport. "Fast spin-up" processes with an Ekman-related solution are halted prematurely. Furthermore, the stagnant, or shutdown, boundary layer, acts as a relatively slippery boundary between the interior flow and its more quickly rotating container, thereby decreasing the rate of momentum diffusion to the interior (*MacReady and Rhines*, 1991; 1993).

3.2 Objectives and Outline of This Chapter

The aim of this chapter is to determine the important spin-up processes in the laboratory when a canyon is not present in the tank topography. Since the laboratory work in this thesis involves an evolving flow over a steep slope, the spin-up behaviour of a fluid over a steep slope must be understood. Although the behaviour of an Ekman layer on a slope has become an area of increasing interest, to date studies have only examined Ekman suction on shallow slopes. This chapter examines the limitations of linear theory for homogeneous Ekman layers over a steep slope, then applies this theory to determine how suction by a sloping Ekman layer will affect laboratory spin-up. Also, spin-up theory for a stratified fluid over a shallow slope is tested to see if its predictions can be extended to steeper slopes. Findings are compared with laboratory results to determine if the theory accurately predicts the spin-up behaviour witnessed in the tank. Results from this chapter will be applied in Chapter 4 to measure the effects of a canyon on flow evolution.

3.3 Spin-up of a Homogeneous Fluid Over a Steep Slope

In the absence of a canyon and stratification, the spin-up process is governed almost purely by Ekman layer dynamics. Radially outward transport is generated in the bottom boundary layer. Continuity dictates that this flow must be balanced by a flux from the interior into the boundary layer and a weak, radially inward flux in the fluid interior (Figure 3.3). As this secondary flow is driven by the boundary layer response to bot-

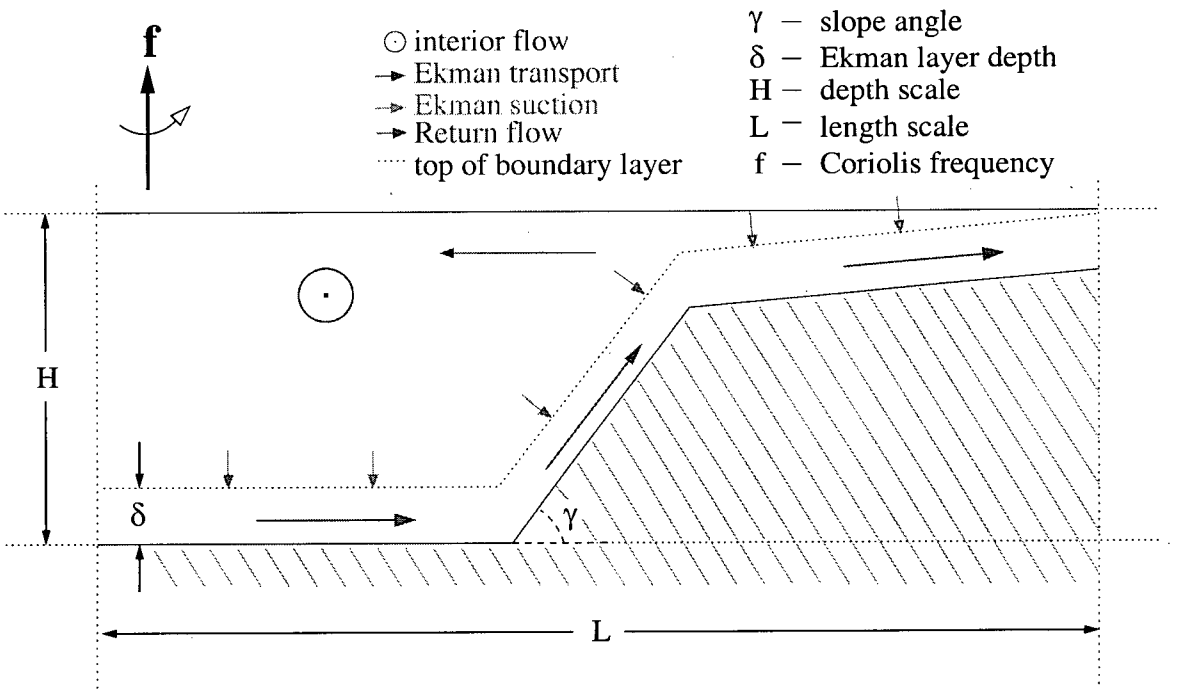

Figure 3.3: Cartoon showing the secondary circulation of a homogeneous fluid in the laboratory.

tom friction, (in this case, over a slope,) analysis begins by examining the momentum equations for a rotating bottom boundary layer on a slope.

3.3.1 Boundary Layer Flow

If the fluid is assumed to be incompressible then the equations of motion and mass conservation in a rotating reference frame are

$$\frac{D\vec{u}}{Dt} + f\hat{k} \times \vec{u} = -\frac{\nabla p}{\rho} + \nu\nabla^2\vec{u}, \tag{3.2}$$

$$\nabla \cdot \vec{u} = 0. \tag{3.3}$$

In these equations $\vec{u}$ is the velocity vector (u, v, w) in Cartesian coordinates (x, y, z), f is the Coriolis frequency which is equal to 2Ω, p is the perturbation pressure equal to the total pressure less the undisturbed hydrostatic pressure ρgz, ρ is the fluid density, g is gravity, ∇ is the gradient vector $(\partial/\partial x, \partial/\partial y, \partial/\partial z)$, D/Dt is the total derivative $\partial/\partial t + \vec{u} \cdot \nabla$, $\hat{k}$ is the unit vector (0,0,1) and ν is the kinematic viscosity of water. Although the problem here involves spin-up over a slope that expresses radial symmetry, an assumption is made that the ratio of the boundary layer height to the radius of curvature is small $O(10^{-2})$, allowing the boundary layer behaviour to be examined in a Cartesian coordinate system.

It is assumed that, at least at lowest order, the flow in the tank, like the topography, is radially symmetric. This allows us to assume $\partial/\partial y$ terms to be small, if not zero. We also assume that in the boundary layer $\partial/\partial x \ll \partial/\partial z$. To study the boundary layer on a slope, it is useful to introduce a rotation of coordinates about the y-axis through the slope angle (Figure 3.4), γ, such that

$$\begin{aligned}
x' &= x\cos\gamma + z\sin\gamma, \quad & x &= x'\cos\gamma - z'\sin\gamma, \\
z' &= z\cos\gamma - x\sin\gamma, \quad & z &= z'\cos\gamma + x'\sin\gamma, \\
u' &= u\cos\gamma + w\sin\gamma, \quad & u &= u'\cos\gamma - w'\sin\gamma, \\
w' &= w\cos\gamma - u\sin\gamma, \quad & w &= w'\cos\gamma + u'\sin\gamma.
\end{aligned}$$

$$\frac{Dw}{Dt} + fv\sin\gamma = -\frac{1}{\rho}\frac{\partial p}{\partial z} + \nu\nabla^2 w. \tag{3.8}$$

The viscous terms in the above equations act as a singular perturbation that is negligible in the fluid interior, but gives rise to the Ekman boundary layers where it is of the same importance as rotation. In the boundary layer, one can neglect the time derivative of the above equations by assuming that the boundary flow remains in a quasi-steady state with the interior flow, which evolves over a larger timescale. Neglecting the time-derivatives results in

$$w\frac{\partial u}{\partial z} - fv\cos\gamma = -\frac{1}{\rho}\frac{\partial p}{\partial x} + \nu\frac{\partial^2 u}{\partial z^2}, \tag{3.9}$$

$$w\frac{\partial v}{\partial z} + f\left(u\cos\gamma - w\sin\gamma\right) = \nu\frac{\partial^2 v}{\partial z^2}, \tag{3.10}$$

$$\frac{1}{2}\frac{\partial w^2}{\partial z} + fv\sin\gamma = -\frac{1}{\rho}\frac{\partial p}{\partial z} + \nu\frac{\partial^2 w}{\partial z^2}. \tag{3.11}$$

The continuity equation is

$$\frac{\partial u}{\partial x} + \frac{\partial v}{\partial y} + \frac{\partial w}{\partial z} = 0. \tag{3.12}$$

It is useful to introduce the scaling, $z = \delta\zeta^*$, $w = \delta(V/L)w^*$, $u = Vu^*$, $v = Vv^*$ and $x = Lx^*$, where $V = \Delta\Omega L$ is the geostrophically balanced interior flow, L is the length scale, and $\delta = \sqrt{2\nu/(f\cos\gamma)}$ is the Ekman layer depth. The asterisks denote non-dimensional variables. The momentum and continuity equations are further treated with the non-dimensional parameters, $R = V/(fL\cos\gamma)$ and $\tan\theta = \delta/L$, where R is a Rossby number and $(\tan\theta)$ is a ratio of the length-to-depth scales used in the problem. This allows us to scale the pressure field as $p = \rho VLf\cos\gamma p^*$. Incorporating these scalings, the momentum equations become (dropping the asterisks)

$$Rw\frac{\partial u}{\partial\zeta} - v = -\frac{\partial p}{\partial x} + \frac{1}{2}\frac{1}{\cos\gamma}\frac{\partial^2 u}{\partial\zeta^2}, \tag{3.13}$$

$$Rw\frac{\partial v}{\partial\zeta} + u - w\tan\gamma\tan\theta = \frac{1}{2}\frac{1}{\cos\gamma}\frac{\partial^2 v}{\partial\zeta^2}, \tag{3.14}$$

$$\frac{R\tan\theta}{2}\frac{\partial w^2}{\partial\zeta} + v\tan\gamma = \cot\theta\frac{\partial p}{\partial\zeta} + \tan\theta\frac{\partial^2 w}{\partial\zeta^2}. \tag{3.15}$$

Further analysis is aided by introducing the asymptotic expansion,

$$(u, v, w) = \sum_{n=0}^{\infty} R^n(u_n, v_n, w_n).$$

For the laboratory setup, $L = 0.5\text{m}$, $f = 0.52\text{s}^{-1}$ and $\nu = 10^{-6}\text{m}^2\text{s}^{-1}$. These values give $\tan\theta = O(R^4)$, allowing us to ignore contributions of this order. The results of (3.15) allow us to determine the vertical variation of the pressure field, which is not of interest for this problem and the equation is dropped from the analysis. Assuming that $\partial p/\partial x$ is balanced by the geostrophic velocity in the interior, and implementing the asymptotic expansion gives, to first order,

$$\begin{bmatrix} 1-v \\ u \end{bmatrix} = \frac{1}{2}\frac{1}{\cos\gamma}\frac{\partial^2}{\partial\zeta^2}\begin{bmatrix} u \\ v \end{bmatrix}, \tag{3.16}$$

which has a classic Ekman spiral solution

$$\begin{bmatrix} u \\ v \end{bmatrix} = A(x)e^{-\sqrt{2\cos\gamma}\zeta}\begin{bmatrix} -\sin\left(\sqrt{2\cos\gamma}\zeta\right) \\ 1-\cos\left(\sqrt{2\cos\gamma}\zeta\right) \end{bmatrix}, \tag{3.17}$$

where $A(x)$ is derived from the geostrophic velocity of the interior and $\partial A/\partial x$ is small.

Continuity is used to determine the flux out of the boundary layer:

$$w = -\int_0^{\infty}\frac{\partial u}{\partial x}d\zeta = \frac{1}{2\sqrt{2\cos\gamma}}\frac{\partial A}{\partial x}. \tag{3.18}$$

If one examines (3.18), it appears that $w \sim \infty$ as $\gamma \to 90°$. This finding is a result of the scaling of w, which also is also dependent on $(\cos\gamma)^{-1/2}$, and signals that at some stage the choice of scales for this problem breaks down. When this breakdown occurs, the results from this solution may no longer be correct. It is necessary, then, to determine

1. whether or not the solution presented is valid for the boundary layer present in the laboratory; and

2. when the solution begins to break down.

As the slope increases, so do the boundary layer thickness ($\delta = \sqrt{2\nu/(f\cos\gamma)}$) and the Rossby number ($R = U/(Lf\cos\gamma)$), which affect the size of $\tan\theta$ and the validity of the asymptotic expansion, respectively.

On the continental slope, ($\gamma = 56°$ and $L = 0.25$ m. For $V = 0.01$ m s^{-1}, $f = 0.52$ s^{-1} and $\nu = 10^{-}6$ m^{2}s^{-1},) $\tan\theta = 0.0026$ and $R = 0.3$. The Rossby number is becoming large and the danger of nonlinearities due to the importance of advective terms looms. Numerical experiments of spin-up over a flat bottom have shown that linear theory holds for Rossby numbers smaller than about 0.5 (*Hart*, 2000; *van de Konijnenberg and van Heist*, 1995). With this information it is reasonable to assume that the behaviour of an Ekman layer on a slope should follow linear theory when $R < 0.5$, so long as $\tan\theta$ remains small (I propose an arbitrary limit of $\tan\theta < 0.05$). For the conditions present in the laboratory, the above solution should hold until the slope reaches about 80° at which point the Rossby number approaches 0.45 and $\tan\theta$ approaches 0.02. This suggests that not only is the solution useful for solving the problem relevant to the laboratory set-up, but that it is well within the domain where its result can be trusted. With this information one can proceed, having faith that the flux into the boundary layer has been properly characterized.

It is now necessary to determine the relation between the right side of (3.18), $\partial A/\partial x$, and the interior flow. This will be done by developing a physical explanation of A, determining its value in the laboratory, and implementing this value into (3.18). In the derivation that has brought us to this point, it has been assumed that although the tank is cylindrical, the boundary layer thickness is small enough that we can ignore any curvature effects and solve the problem in Cartesian coordinates. While defining A, Cartesian coordinates will remain in use even though the following explanation takes

place in the interior. Once a physical description of A is made, its value with respect to the cylindrical coordinate system is easily defined.

To understand the physical meaning of A, begin by considering an infinitely long, sloping boundary of angle γ below a half-space of homogeneous fluid on an f-plane. The fluid has an along slope velocity, $v(x)$, with a horizontal shear (Figure 3.5a). If the velocity had a cross slope component to it as well, the curl of this velocity field normal to the boundary would be $\partial v/\partial x' - \partial u/\partial y$ but as there is no u-component here, it is simply $\partial v/\partial x'$. If the fluid is assumed to be inviscid except at the bottom where it interacts with the sloping boundary, then the boundary layer will respond to the component of the curl whose direction is normal to its plane, i.e. $(0, 0, \partial v/\partial x')$, but not those which lie in its plane, i.e. $(-\partial v/\partial z', 0, 0)$, (Figure 3.5b). This relationship implies that as γ increases, the amount of shear that contributes to the boundary layer evolution will decrease as $\cos\gamma$.

Returning to the laboratory setting, imagine that $v(r)$ is the along-slope velocity in the interior. v can be non-dimensionalized as $VA(r)$, where V is a characteristic velocity of the interior, and $A(r)$ is the non-dimensional velocity present in (3.18). This definition lets us rewrite (3.18) as

$$w = \frac{1}{2\sqrt{2\cos\gamma}} \cos\gamma \nabla \times A(r), \tag{3.19}$$

or, in dimensional coordinates,

$$w = \frac{1}{2}\sqrt{\frac{\nu}{f}} \nabla \times v^i \tag{3.20}$$

where v^i is the velocity in the interior.

This result states that the slope angle has no effect on the flux out of the boundary layer, which may be surprising. However, if one considers that the total frictional drag imposed by the boundary layer over a given horizontal section will be increased by a factor of $\sec\gamma$ but that the effective value of the Coriolis frequency in the boundary layer

will be decreased by a factor of $\cos\gamma$, then the result is less worrisome.

3.3.2 Effect of a Slope on Ekman Suction

For small γ, it is often assumed that $\sin\gamma \approx 0$, $\cos\gamma \approx 1$, and the vertical component of Ekman suction is equal the total Ekman suction calculated over a given region. For steeper slopes, these assumptions do not hold. As the slope increases, the vertical flux into the boundary layer decreases as $\cos\gamma$ (Figure 3.6). When $\sin\gamma$ is large, Ekman suction will invoke a radially outward flow in the interior. For these laboratory experiments, it is assumed that horizontal flows due to Ekman suction are small and can be ignored for the desired accuracy of solution. The expected impact of a sloping boundary layer on the the vertical flux from the interior is shown in Figure 3.7. This flux, which is a function

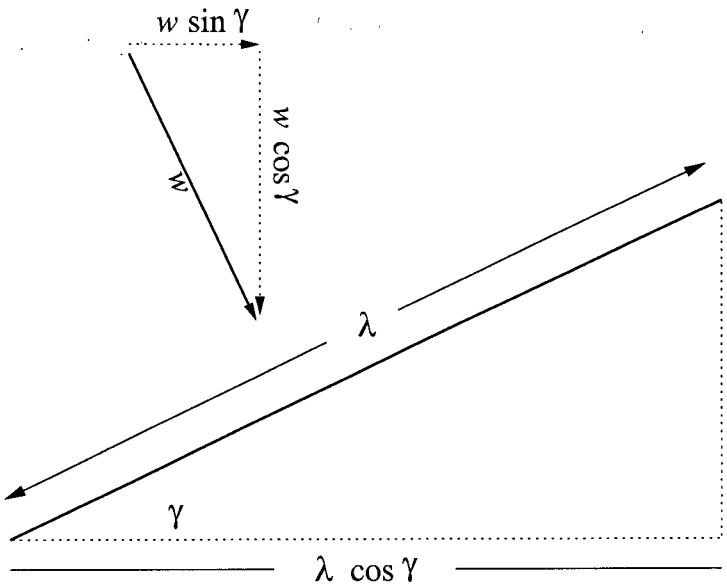

Figure 3.6: Vertical velocity contribution to Ekman suction on a slope.

of the interior flow, is responsible for the non-canyon and non-diffusive spin-up processes.

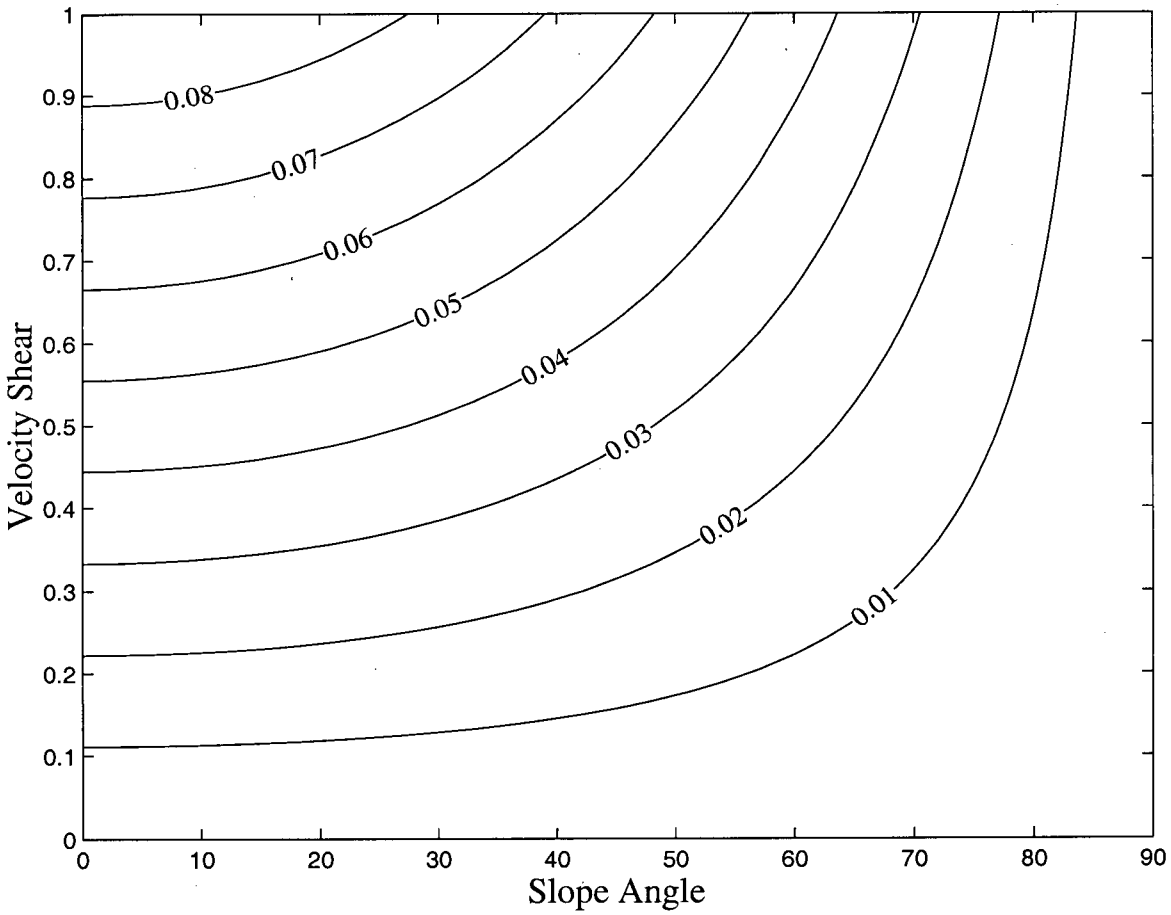

Figure 3.7: Vertical component of Ekman pumping into a sloped boundary layer (i.e. vertical flow *into* the Ekman layer, *not* the flow *normal to* the boundary layer) is a function of slope angle and shear. Vertical velocities are exaggerated by a factor of 10^{-3}. The angle to which this relationship remains valid is dependent on the geometry of the problem. For the laboratory set-up, the solution is expected to hold until γ reaches an angle of about 80°.

3.3.3 Effect of Ekman suction on Spin-up

Once the flux into the boundary layer is determined, the next step is to understand how this flux will affect the evolution of flow in the tank. In the interior of the fluid, friction is negligible and at first order potential vorticity is conserved, i.e.,

$$\frac{D}{Dt}\left(\frac{f+\nabla\times\vec{u}_H^i}{H}\right)=0 \tag{3.21}$$

where H is the water depth, and $\vec{u}_H^i$ corresponds to the horizontal velocity field. The superscript, i denotes that these are values for the interior. (3.21) can be expanded to yield

$$\frac{1}{H}\frac{D}{Dt}\left(f+\vec{u}_H^i\right)+\left(f+\vec{u}_H^i\right)\frac{D}{Dt}\frac{1}{H}=0. \tag{3.22}$$

Although it may seem that H is a constant, it should be remembered that if there is a vertical flux out of the water column, this is equivalent to a change in depth. Hence, $\partial H/\partial t = w^i$. Assuming that f is a constant and that nonlinear terms can be ignored, then (3.22) becomes

$$\frac{\partial}{\partial t}\nabla\times\vec{u}_H^i=\frac{w^i}{H}\left(f+\nabla\times\vec{u}_H^i\right), \tag{3.23}$$

where

$$w^i = w\cos\gamma=\sqrt{\frac{\nu\cos^2\gamma}{4f}}\left(\nabla\times\vec{u}_H^i\right), \tag{3.24}$$

$$\nabla\times\vec{u}_H^i=\frac{1}{r}\frac{\partial}{\partial r}(rv) \tag{3.25}$$

and v is the azimuthal (along slope) geostrophic velocity. (Figure 3.6).

In the classic spin-up experiments with a flat bottom, $\nabla\times\vec{u}_H^i$ decays exponentially in time, with no added spatial variation (i.e. $\nabla\times\vec{u}_H^i=[\nabla\times\vec{u}_H^i]_o\exp(-t/\tau)$, where τ is the appropriate timescale). Due to the depth variation present in the laboratory set-up of these experiments, it is difficult give a classical spin-up timescale. During the time over which the ramping of the table takes place alone, the strong depth changes within the

tank cause the velocity structure to deviate from a linear dependence on the radius like that seen in the classic spin-up experiments (Figure 3.8). Spin-up over a slope cannot be easily solved by analytical techniques due to spatial variation in topography, and the problem is solved numerically.

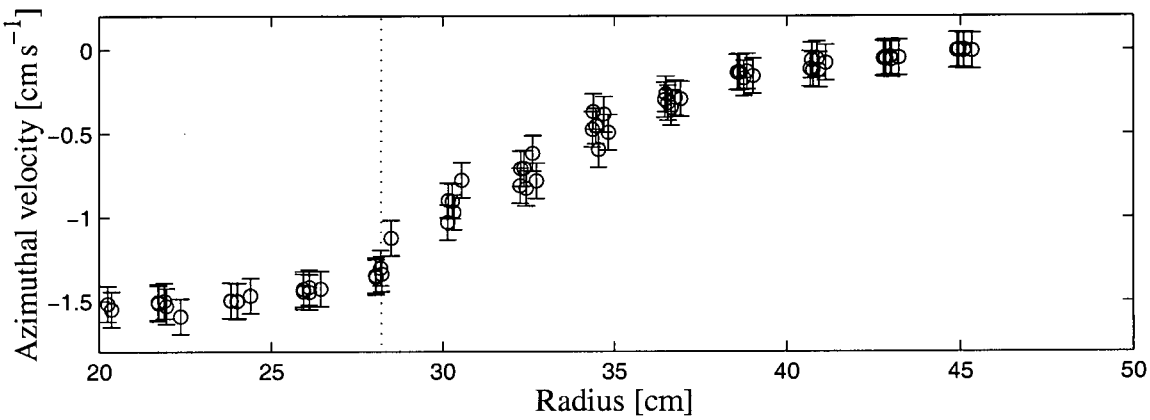

Figure 3.8: Example of the surface velocity in the tank sampled immediately after ramping of the rotation rate of the table. The dotted line at $r = 28.2$ cm represents the location of the shelfbreak. The tank edge is at $r = 50$ cm. In the classic spin-up problem, the azimuthal velocity follows $u = \alpha r$, where α is dependent only on time.

3.3.4 Solving the Homogeneous Problem Numerically

Laboratory results suggest that (3.23) is not separable, and the equations are solved numerically. Determining how the velocity field will evolve over a given time requires three steps that must be iterated through the appropriate number of time steps:

1. the horizontal structure of the vertical velocity field, defined by (3.24), must be solved;

2. how the vertical velocity (and diffusion for stratified trials) affects the evolution of vorticity, defined by (3.23), must be determined; and

3. the velocity must be found by integrating its curl.

(3.24) and (3.23) solve the homogeneous system.

The solution to the above problem is solved over the radial domain r = [25 cm, 45 cm], with a spatial resolution $\Delta r = 2$ mm and a temporal resolution $\Delta t = 0.1$ s. The initial condition required for the problem is the velocity in the interior, which is set based on laboratory observations. The boundary conditions are no-slip and free-slip at the inner- and outer-edges of the radial domain, respectively. Topography in the numerical model is relatively simple: the continental slope is inclined at 56° and the continental shelf has a grade of approximately 4.5° (Figure 3.9).

The method for finding the value of w is straight forward. Discretizing (3.24) in cylindrical coordinates gives

$$w_{(n,t)} = \cos\gamma_n \sqrt{\frac{\nu}{4f}} \left(\frac{v_{(n+1,t)} + v_{(n,t)}}{r_{n+1} + r_n} + \frac{v_{(n+1,t)} - v_{(n,t)}}{\Delta r} \right), \tag{3.26}$$

where the terms here are the same as those defined in (3.24) and the subscripts n represent the discretized locations in space over the r-domain (r_1 = 25 cm, r_2 = 25 cm + Δr, etc.), the subscripts t represent discretized locations in time over the t-domain (t_1 = 0 s, t_2 = 0 s + Δt, etc.), at t_t and $v_{(n,t)} = v(r_n)$ at t_t. (3.26) gives values for w for $n = 1, 2, 3, 4, ..., N-1$.

Once the $w_{(n,t)}$ is determined, v is calculated a time-step Δt forward in time. (3.23) is discretized to give

$$\Delta(rv)_{(n,t+1)} = \frac{2w_{(n,t)}}{H_{n+1} + H_n} \left(f + \frac{v_{(n+1,t)} + v_{(n,t)}}{r_{n+1} + r_n} + \frac{v_{(n+1,t)} - v_{(n,t)}}{\Delta r} \right) \frac{r_{n+1} + r_n}{2} \Delta t \Delta r, \tag{3.27}$$

where $\Delta(rv)_{(n,t)}$ is equal to $\Delta(rv)_{(n,t)} = r_{n+1}v_{(n+1,t)} - r_n v_{(n,t)}$ after the time-step, Δt. The expression defining $\Delta(rv)_n$ can be rearranged to give the solution for v

$$v_{(n,t)} = \left(v_{(n+1,t)} r_{n+1} - \Delta(vr)_{(n,t)} \right) \frac{1}{r_n} \tag{3.28}$$

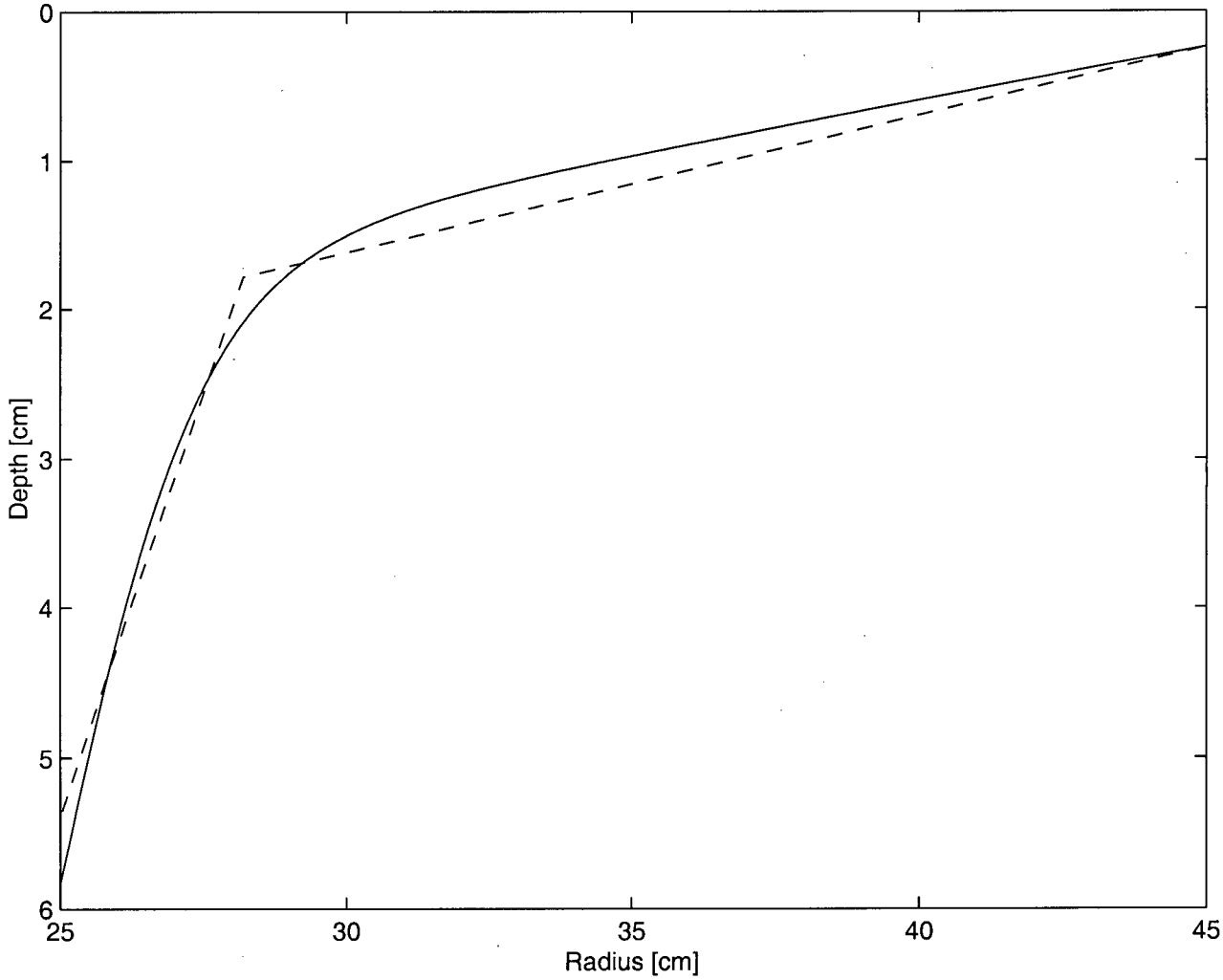

Figure 3.9: Topography present in the laboratory (solid line) and that used to test the theoretical model (dashed line).

To match the boundary condition, the integrations are done from high values of n to low ones, i.e. $n = N-1, N-2, \ldots, 1$, using the boundary condition $v_N = 0$. Theoretical expectations developed are compared to laboratory results, but the method for determining initial conditions must first be discussed.

3.3.5 Comparing Theoretical Predictions To Laboratory Results

In order to compare the theoretical predictions to measurements from the laboratory, it is necessary to match the initial velocity. For the laboratory experiments, time is set to zero at the end of the forcing period. Flow evolution early in the ramping period is difficult to characterize as can be seen from laboratory data (Figure 3.10). Rather than attempting to solve for the velocity evolution over the ramping period, I chose to match the initial conditions to the measured velocity at the end of the forcing period. Unfortunately, the tank was not completely level, and this lead to a periodic oscillation in the flow field. In order to be consistent in measurements, I sampled velocities in the bottom of the first wave-trough after the end of forcing as it passed through the measurement area. Other obvious alternatives include sampling in the crest of the wave or at the node of the wave (when the velocity anomaly was equal to zero). The first alternative was rejected primarily because cross-shelf velocities were present near the edge of the tank during wave crest. The second was rejected because the rate of wave change is fastest at that time, and consistent identification of this location in time was challenging.

3.3.6 Fitting Curves to the Velocity Data

Once a location in time is selected, the velocity curve is fit to *all* data within the measurement window with the restriction of $r > 20$ cm. This was done because the numerical solutions to the spin-up equations described in sections §3.3 and §3.4 extended from

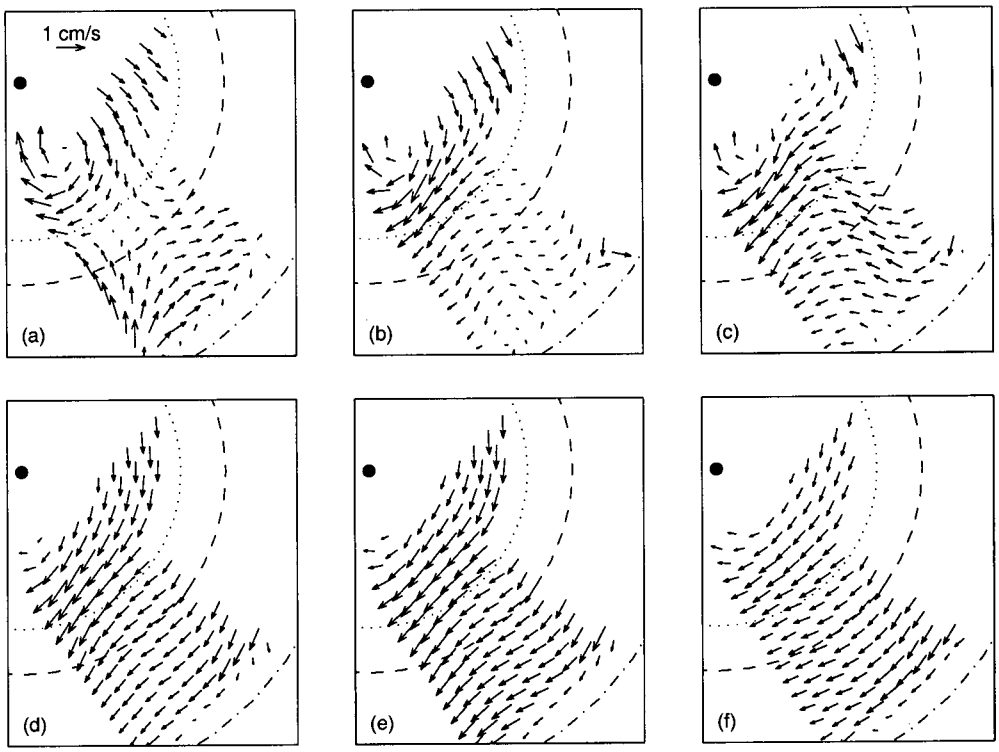

Figure 3.10: Laboratory measurements showing nonlinear spin-up in early time. Velocity fields shown are (a) 1 seconds, (b) 3 seconds, (c) 5 seconds, (d) 7 seconds, (e) 9 seconds and (f) 11 seconds after ramping begins. The ramping trime is 27.3 seconds. The large dot represents the middle of the tank. The beginning of the continental slope (dotted line, $r = 22$ cm), the shelfbreak (dashed line, $r = 28.2$ cm) and $r = 45$ cm (dashed-dotted line) are shown to aid in spatial orientation of the image. Ideally, the velocity would be near 0 in figure (a). The disturbances in the flow field are likely due to the oscillation present in the tank, deviation from initial solid body rotation or non-linear effects in spin-up.

$r = 45$ cm to $r = 25$ cm. The data were fit to a fourth order polynomial that was forced to match the boundary condition, $v(r = 50\text{cm}) \equiv 0$, i.e. the curve of best fit is equal to

$$V(r) = C_1(r - 50) + C_2(r - 50)^2 + C_3(r - 50)^3 + C_4(r - 50)^4, \tag{3.29}$$

where the constants C_1, C_2, C_3 and C_4 are determined by a least-squares approximation. (3.29) can be rewritten in matrix form as $V_{1\times N} = R_{4\times N}C_{1\times 4}$. The solution for $C_{1\times 4}$ is found by matrix manipulation:

$$C = (R'R)^{-1}R'\tilde{V} \tag{3.30}$$

where R' is the transpose of R. Once C is found, a new matrix $\hat{R}$, which represents the radial points in the finite difference numerical schemes, is used to determine the initial condition of the numerical solution, $\hat{V}$.

Although the value of C is found, it leaves an important question unanswered, namely, "what is the error in the approximation?" This question can be answered in several ways. One option is to follow the the error propagation from measurements of $\tilde{V}$ to C in (3.30). But this method gives the errors in the individual constants, rather than our exact uncertainty in the line the data have produced.

As a result, an alternative method was used to determine the error. Following a suggestion in §14.5 of *Press et al.* (1986) it is assumed that the values collected in $\hat{V}$ are close enough to the real values that the error in $\tilde{V}$ has a normal distribution. For this reason, a bootstrap-like method was used in determining error estimates. A random selection of 100 points were taken from the laboratory data (whose number ranged from 110 to 172 points) and each had a (normally distributed) random error added to it. The value of C is recalculated in 100 iterations as

$$C^i = (R'R)^{-1}R'(\tilde{V}^i + Q^i\delta\tilde{V}), \tag{3.31}$$

where $\tilde{V}^i$ is a random set of $\tilde{V}$ and $Q^i_{1\times N}$ is a normally distributed set of random numbers ranging from -1 to 1 that is reevaluated for each iteration.

The values for the constants, C^i, are then each used to individually determine a set of vectors $\hat{V}^i$. A value $\hat{V}$ is determined as

$$\hat{V} = \frac{1}{100}\sum_{i=1}^{100}\hat{V}^i$$

with the error being twice the standard deviation from the mean.

3.3.7 Flow Comparisons For the Homogeneous Spin-up Model

A comparison of actual flow evolution to its theoretical expectation is shown in Figure 3.11. Laboratory and theoretical results are shown at 5 second intervals. The data represented in the plot are from an angular section of the tank (the same region illustrated in Figure 3.10).

3.4 Spin-up of a Stratified Fluid Over a Steep Slope

In this section, the theory developed in §3.3 is extended to include stratification. The previous analysis showed that Ekman suction in a homogeneous fluid over a steep slope can be calculated with relative ease. This finding is now employed as an assumption for the stratified fluid case. When stratification is introduced, however, the upslope transport that is present in the sloped Ekman layer redistributes the density field, advecting denser fluid into a regime of less dense fluid. This introduces buoyancy forces, which eventually become as large as Coriolis forces, effectively shutting down the boundary layer and insulating the interior from the bottom.

Although an analytical model for this problem cannot be easily attained due to buoyancy effects in the equations of motion on a steep slope, laboratory results are predicted

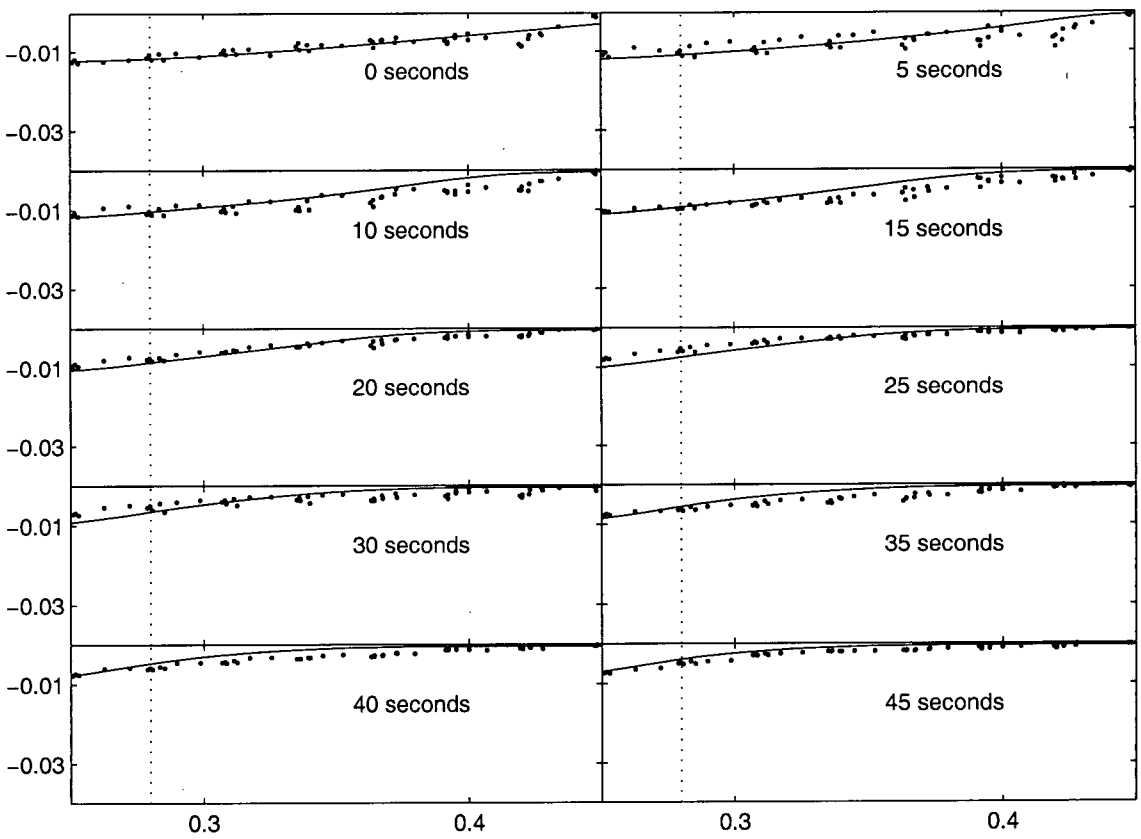

Figure 3.11: Spin-up of a homogeneous fluid ($f = 0.52$ s-1, $\Delta f = 0.12$ s-1) without a canyon, comparison of laboratory observations (dots) to theoretical predictions (lines). Error on data and line are only slightly larger than points and line thickness. The location of the shelfbreak is shown as a dotted line at $r = 22$ cm. Time slices are shown every 5 seconds. One rotation period is 24.2 seconds.

by a diffusion model that is based on the work of *MacCready and Rhines* (1991) and the theory introduced in the previous section. *MacCready and Rhines* (1991) predict the shutdown time, τ, for a bottom Ekman boundary layer over a gentle slope to be $\tau = S/[(1+S)S^2 f\cos\gamma]$, where $S = (N\sin\gamma/f\cos\gamma)^2$ is a Burger number and N is the Brunt-Väisälä frequency. When shutdown of the boundary layer is complete, it insulates the interior from the friction effects of the bottom. In this limit there is no Ekman suction and flow evolution will evolve as (after *MacReady and Rhines*, 1991):

$$\frac{\partial v}{\partial t} + u\frac{\partial v}{\partial r} + fu = \nu\left(\sin^2\gamma + \frac{S}{1+S}\cos^2\gamma\right)\frac{\partial^2 v}{\partial z^2} + \nu\left(\frac{S}{1+S}\sin^2\gamma + \cos^2\gamma\right)\nabla_H^2 v, \quad (3.32)$$

where z is vertical (i.e. not normal to the slope) and ∇_H^2 represents the horizontal components of the Laplacian operator, and u is the radial velocity. Horizontal diffusion is not included in the model of *MacCready and Rhines* (1991) but must be considered for this problem. Near the shelfbreak, the depth change is rapid enough that a horizontal shear will evolve in the flow, requiring the consideration of horizontal diffusion for the problem. For a no-slip bottom boundary and only vertical diffusion, this suggests a spin-up timescale of 15 minutes for water only 1 cm seaward of the shelfbreak, compared with about 8 minutes if horizontal diffusion is included.

For laboratory simulations, the shutdown timescale over the continental shelf ranged from 2 seconds ($f = 0.52\text{s}^{-1}$, $N = 4.4\text{s}^{-1}$) to 20 seconds ($f = 0.52\text{s}^{-1}$, $N = 2.2\text{s}^{-1}$). (For $f = 0.52\text{S}^{-1}$, one inertial period is equal to 12 seconds.) This shutdown process is a gradual one suggesting that Ekman suction into the boundary layer, and therefore its corresponding spin-up influence, will be important early in time but will decay on the shutdown timescale. Flux out of the boundary layer will then be a slightly altered version of (3.24):

$$w_B = \sqrt{\frac{\nu\cos^2\gamma}{4f}}\left(\nabla\times\vec{u}_B^{\,i}\right)\exp\left(-\frac{t}{\tau}\right) \quad (3.33)$$

where w_B is the vertical Ekman flux out of the boundary layer and $\vec{u}_B^{\,i}$ is the horizontal

velocity of the interior along the tank bottom. It is assumed that the Ekman suction of the stratified boundary layer is the same as that for the non-stratified Ekman layer, except that it decays exponentially in time on the shutdown timescale. Following (3.23), it is anticipated that the flow evolution due to Ekman effects is

$$\frac{\partial}{\partial t}\nabla \times \vec{u}_H^i = \frac{w^i(t)}{H}\left(f + \nabla \times \vec{u}_H^i\right) \tag{3.34}$$

A similar approach is taken to characterize the evolution of the diffusive behaviour in the fluid. Early in time, the familiar "isotropic diffusion" is present:

$$\nu\nabla^2\vec{u}_H^i. \tag{3.35}$$

By the end of boundary layer shutdown, however, the diffusion will follow (3.32). The formation of this shutdown boundary layer is due to the gradual increase in gravitational force imposed on the fluid as it is advected upslope. As such, it can be expected that the diffusion will change from (3.35) to (3.32) over the shutdown timescale:

$$\frac{\partial \vec{u}_H^i}{\partial t} + u\frac{\partial \vec{u}_H^i}{\partial r} + f\hat{k} \times \vec{u}_H^i = \nu\left\{\exp\left(-\frac{t}{\tau}\right)\nabla^2 + \left[1 - \exp\left(-\frac{t}{\tau}\right)\right]\right.$$
$$\left.\left[\left(\sin^2\gamma + \frac{S}{1+S}\cos^2\gamma\right)\frac{\partial^2}{\partial z^2} + \left(\frac{S}{1+S}\sin^2\gamma + \cos^2\gamma\right)\left(\frac{1}{r}\frac{\partial}{\partial r} + \frac{\partial^2}{\partial r^2}\right)\right]\right\}\vec{u}_H^i \tag{3.36}$$

From conservation of mass, $\nabla_H \cdot \vec{u_h} = -\partial w/\partial z$ which, given uniform stretching through the water column due to Ekman suction is $-w^i(t)/H$. Therefore $\nabla\times$ (3.36) can be written as

$$\left\{\frac{\partial}{\partial t} - \nu \exp\left(-\frac{t}{\tau}\right)\nabla^2 - \nu\left[1 - \exp\left(-\frac{t}{\tau}\right)\right]\left[\left(\sin^2\gamma + \frac{S}{1+S}\cos^2\gamma\right)\frac{\partial^2}{\partial z^2}\right.\right.$$

$$\left.\left. + \left(\frac{S}{1+S}\sin^2\gamma + \cos^2\gamma\right)\left(\frac{1}{r}\frac{\partial}{\partial r} + \frac{\partial^2}{\partial r^2}\right)\right]\right\}\nabla \times \vec{u}_H^i = \frac{w^i(t)}{H}\left(f + \nabla \times \vec{u}_H^i\right). \quad (3.37)$$

The theory of *MacCready and Rhines* (1991) being applied to model spin-up is derived to work only on gentle slopes. Due to the lack of a theory describing arrested or shutdown boundary layers on a steep slope, it is assumed here that the general theory of *MacCready and Rhines* (1991) adequately characterizes the behaviour of the shutdown Ekman layer over a steep slope. Applying this theory to the steep continental slope gives a shutdown timescales of $O(10^{-2}\text{s})$. This short timescale suggests that even if shutdown on steep slopes occurs considerably more slowly than on gentle slopes, then the boundary layer will have shut down by the time the ramping of the tank velocity is complete.

As in the homogeneous case, the initial conditions are set from the laboratory flow. This poses a slight problem: the flow below the surface is unknown as its vertical structure varies in time. As a result certain assumptions must be made to set the boundary conditions. The first is that effects from Ekman suction are vertically homogeneous. While stratification does have an effect on varying the Ekman flux, it is small over the depths being considered in this study. The second assumption is that over the time of the experiments, diffusive effects from the shutdown boundary layer barely alter the flow. These assumptions were tested by examining the vertical evolution of the flow with time in the numerical model. (Originally vertical variation in Ekman suction was considered, but its impact on flow evolution was negligible.) When model predictions are compared with actual laboratory output (see §3.3.5), the agreement suggests that these assumptions are acceptable.

Equation (3.37) is solved numerically with boundary conditions of no-slip at the outer

radial edge of the modeling domain and along the bottom, and free-slip along the top and along the inner radial edge of the modeling domain.

3.4.1 Solving the Stratified Problem Numerically

The method for determining the result to (3.37) is indeed similar to that used for (3.23) in §3.3 except that for the stratified solution vertical variation and diffusion are present. This alters the method of solution to

1. determine the vertical velocity;
2. use Ekman suction and diffusion to evaluate the time-evolution of the velocity curl; and
3. calculate the velocity from the velocity curl.

The problem is solved over the radial domain r = [25 cm, 49 cm], with a spacing, $\Delta r = (49 - 25)/99$ cm, the vertical domain z = [0 cm, 6 cm], with a spacing, $\Delta z = \Delta r$, where $z = 0$ is at the surface, and the temporal domain t = [0 s, T], with a spacing $\Delta t = 0.0625s$.

Vertical velocity is determined by (3.33) using the same discretized form as (3.26):

$$w_{(n,t)} = \cos\gamma_n \sqrt{\frac{\nu}{4f}} \left(\frac{v_{(H_{n+1},n+1,t)} + v_{(H_n,n,t)}}{r_{n+1} + r_n} + \frac{v_{(H_{n+1},n+1,t)} - v_{(H_n,n,t)}}{\Delta r} \right) \exp\left(\frac{2t}{\tau_{n+\frac{1}{2}}} \right), \tag{3.38}$$

where the subscripts n and t are the same as §3.3.4, the subscript H_n represents the bottom-most vertical layer within the model, i.e. the layer below-which the coordinates have left the fluid and are beyond the boundary (Fig. 3.12), and $\tau_{n+\frac{1}{2}}$ is the shutdown timescale at $r_{n+\frac{1}{2}}$, where $r_{n+\frac{1}{2}} = (r_{n+1}+r_n)/2$. From hence forth, values at the discretized step $n+\frac{1}{2}$ are equal to the average of the two bounding values at n and $n+1$. The Ekman layer is not explicitly present in the model.

where

$$(\nabla \times \vec{u})_{q,n+\frac{1}{2},t+1} = \frac{2}{r_{n+1}+r_n}\frac{v_{q,n+1,t+1}r_{n+1} - v_{q,n,t+1}r_n}{\Delta r}. \tag{3.42}$$

Note that the subscript q is being used in the place of H_n in these diffusion terms. The subscript q represents the discretized locations within the z-domain (i.e. $z_1 = 0$ cm, $z_2 = 0$ cm $+ \Delta z$, etc.). H_n marks a special value of q at each radial location r_n. H_n holds the bottom element in the z-coordinate that is still within the fluid. Using these abbreviations allows the discretized form of (3.37) to be written as

$$\frac{(\nabla \times \vec{u})_{q,n+\frac{1}{2},t+1} - (\nabla \times \vec{u})_{q,n+\frac{1}{2},t}}{\Delta t} = \frac{w_{n,t}}{H}[f + (\nabla \times \vec{u})_{q,n+\frac{1}{2},t}] + \left\{\nu \exp\left(-\frac{t}{\tau_{n+\frac{1}{2}}}\right)\right.$$

$$\left. +\nu\left[1 - \exp\left(-\frac{t}{\tau_{n+\frac{1}{2}}}\right)\right]\left(\sin^2\gamma_{n+\frac{1}{2}} + \frac{S_{n+\frac{1}{2}}}{1+S_{n+\frac{1}{2}}}\cos^2\gamma_{n+\frac{1}{2}}\right)\right\}\Delta_{zz}(\nabla \times \vec{u})_{(q,n+\frac{1}{2},t)}$$

$$+\left\{\nu \exp\left(-\frac{t}{\tau_{n+\frac{1}{2}}}\right) + \nu\left[1 - \exp\left(-\frac{t}{\tau_{n+\frac{1}{2}}}\right)\right]\left(\frac{S_{n+\frac{1}{2}}}{1+S_{n+\frac{1}{2}}}\sin^2\gamma_{n+\frac{1}{2}} + \cos^2\gamma_{n+\frac{1}{2}}\right)\right\}$$

$$\left(\frac{\Delta_r(\nabla \times \vec{u})_{(q,n+\frac{1}{2},t)}}{r_n} + \Delta_{rr}(\nabla \times \vec{u})_{(q,n+\frac{1}{2},t)}\right) \tag{3.43}$$

The velocity can then be back-calculated out of $(\nabla \times \vec{u})_{n,q,t+1}$:

$$v_{n,q,t+1} = \left[-\frac{(\nabla \times \vec{u})_{q,n+\frac{1}{2},t+1}(r_{n+1}+r_n)\Delta r}{2} + v_{n+1,q,t+1}r_{n+1}\right]\frac{1}{r_n}. \tag{3.44}$$

As the boundary condition states that $v_{N,q,t} \equiv 0$, v is calculated by means of (3.44) starting at $n = N-1$ and traveling radially inward.

3.4.2 Flow Comparison For the Stratified Spin-up Model

Using the same methods for determining initial conditions as described in §3.3.6, the model for stratified spin-up can be tested as well. The following figures (Figure 3.13 through Figure 3.17) show laboratory and theoretical results at 5 second intervals. The

data represented in these plots are from an angular section of the tank (the same region illustrated in Figure 3.10). As there is a wave traveling through the tank, this can sometimes cause local variations in the velocity field. A good example of this can be seen in the 10th panel (45 second-panel) of Figure 3.14. Another effect of this wave is directly linked to the sampling strategy. As mentioned in §3.3.6, the choice of temporal location for capturing the initial conditions was done so as to be at the trough of each wave. As a result, one can see in almost all comparisons that the prediction leads the laboratory initially, but that after one rotation period, the two match together again relatively well. It is the comparison between theory and lab after one rotation period that is important.

Although there is a tendency for the velocity near the edge of the tank to approach zero faster in the theoretical expectations than in the laboratory results, the final implications of this are not severe, as is explained in greater detail in the following chapter.

3.5 Summary

This chapter examines spin-up of a both homogeneous and stratified fluids in laboratory when a canyon is absent. The theory of how the boundary layer will evolve over a steep slope is examined, and the Ekman suction over the slopes present in laboratory topography is found. Analysis of the solution suggests that, so long as the Rossby number stays below 0.5 and the ratio of Ekman layer depth to the characteristic lengthscale of the interior is small, the flux into the Ekman layer will follow linear theory. As the slope of the boundary increases, the proportion of this flux that results in vortex tube stretching of the interior decreases as the cosine of the slope angle.

Introduction of stratification to the fluid in the laboratory results in a transport of dense water upslope, which leads to the development of buoyancy forces in the boundary layer. Eventually the buoyancy effects match rotation and the bottom boundary layer

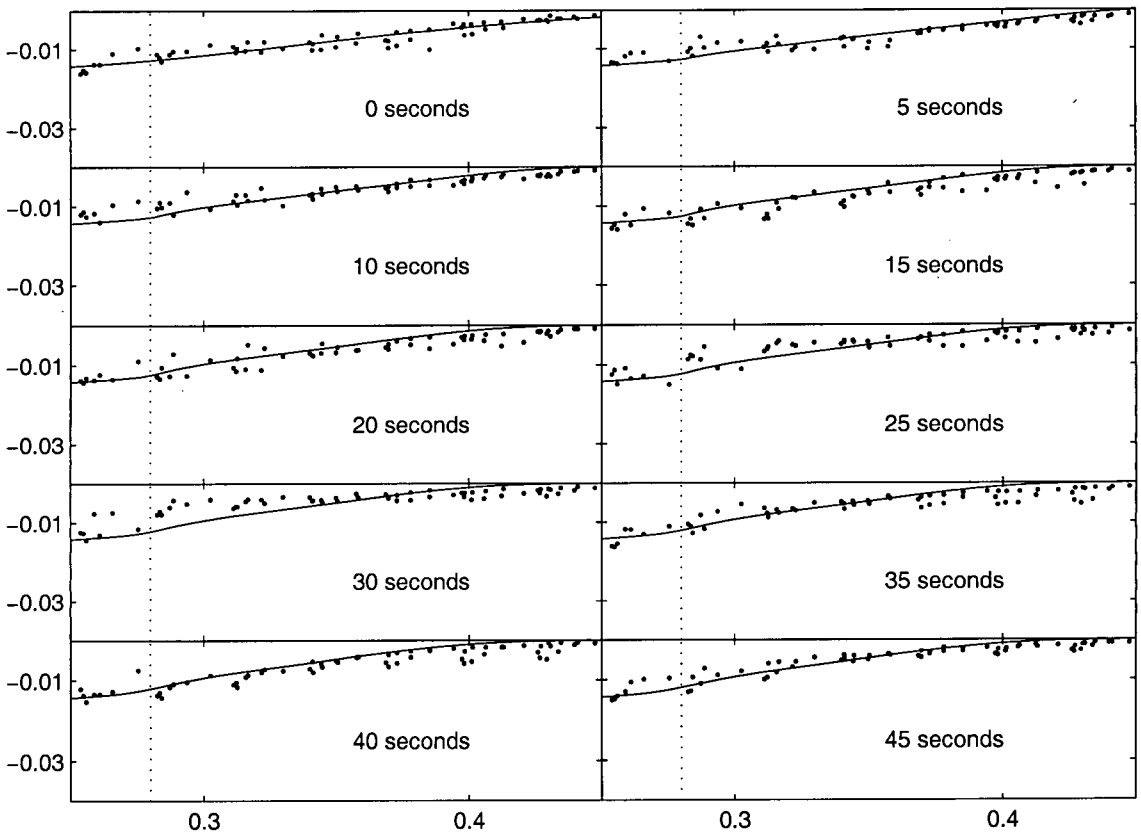

Figure 3.13: Spin-up for trial 1 ($N = 2.2$ s^{-1}, $f = 0.52$ s-1, $\Delta f = 0.12$ s-1) without a canyon, comparison of laboratory observations (dots) to theoretical predictions (lines). Error on data and line are only slightly larger than points and line thickness. The location of the shelfbreak is shown as a dotted line at $r = 22$ cm. Time slices are shown every 5 seconds. One rotation period is 24.2 seconds.

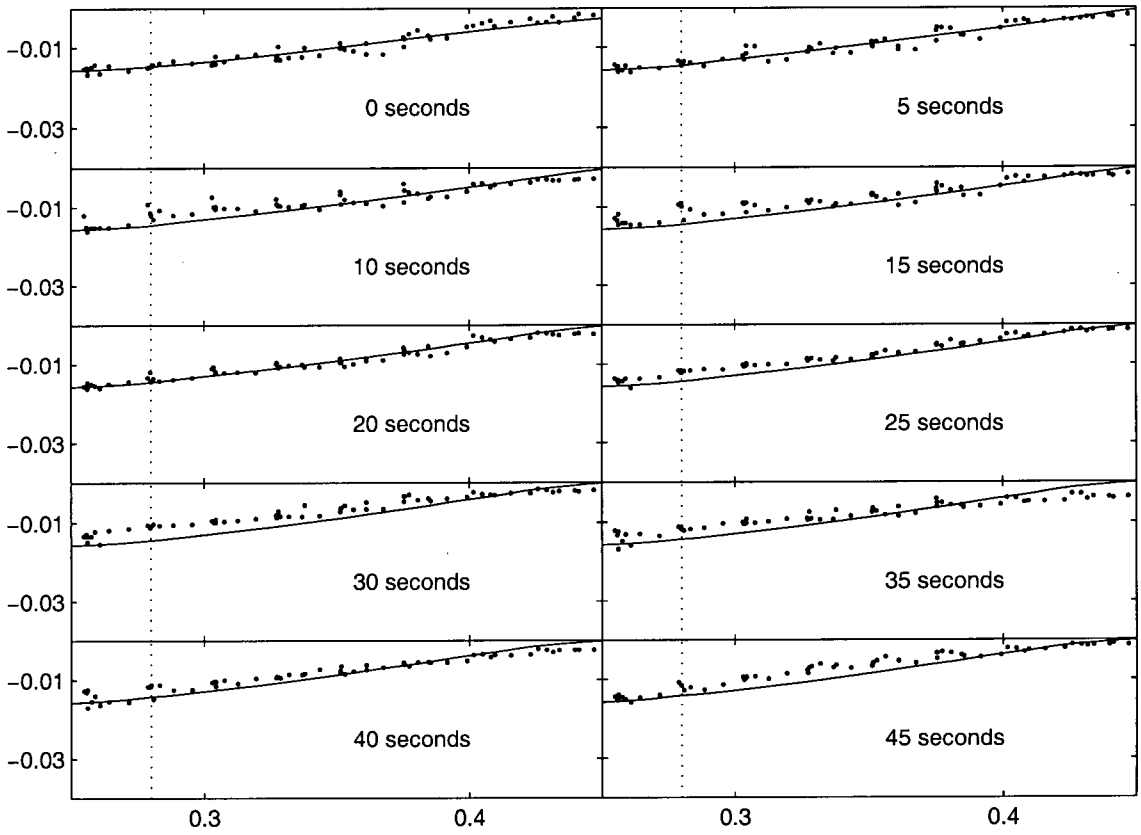

Figure 3.14: Spin-up for trial 4 ($N = 4.4$ s^{-1}, $f = 0.52$ s-1, $\Delta f = 0.12$ s-1) without a canyon, Plots are the same as Figure 3.13. One rotation period is 24.2 seconds.

shuts down, arresting all Ekman suction and, therefore, vortex tube stretching. The boundary layer acts as an insulator between the interior and the bottom boundary. Spin-up continues to take place by diffusion, although at a decreased rate due to the insulated boundary. Laboratory results match well with theoretical expectations of flow evolution. Despite the presence of a wave traveling in the tank with a period of $4\pi f^{-1}$, theoretical prediction of the flow still match with laboratory data when the two are compared one wave period after modeling begins.

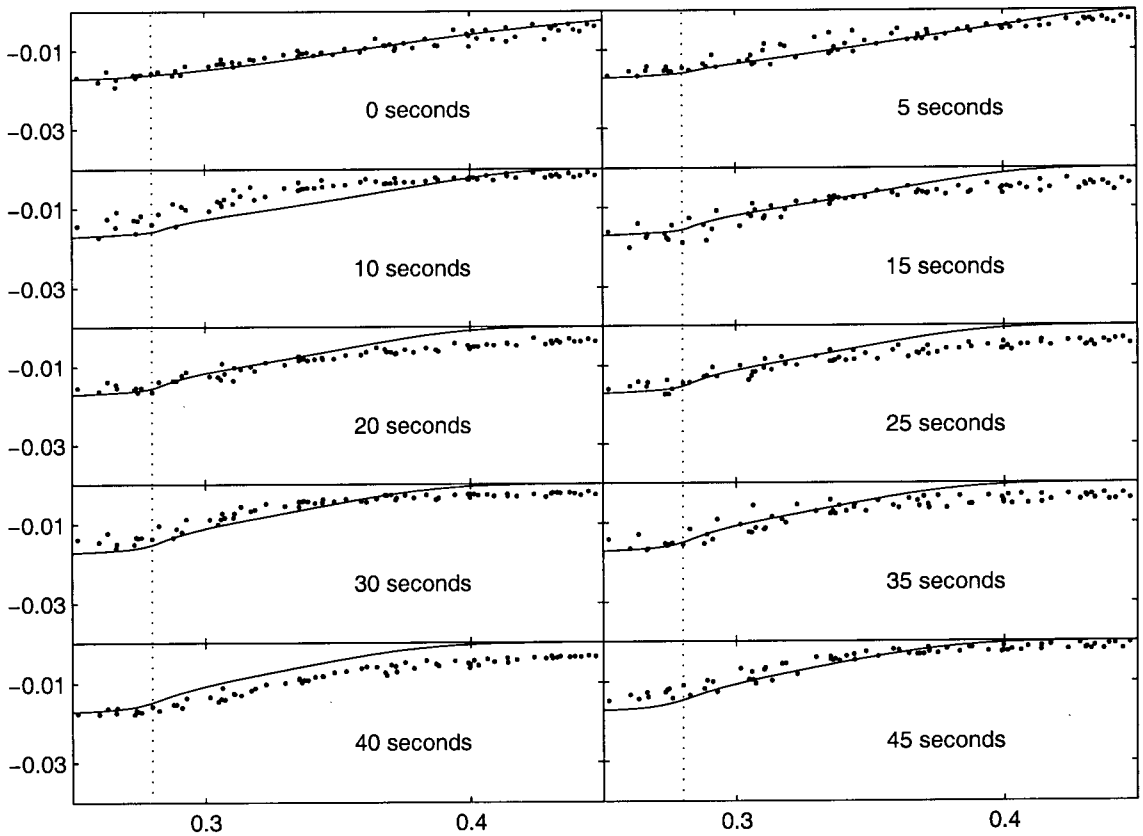

Figure 3.15: Spin-up for trial 6 ($N = 2.2$ s^{-1}, $f = 0.7$ s-1, $\Delta f = 0.12$ s-1) without a canyon, Plots are the same as Figure 3.13. One rotation period is 18.0 seconds.

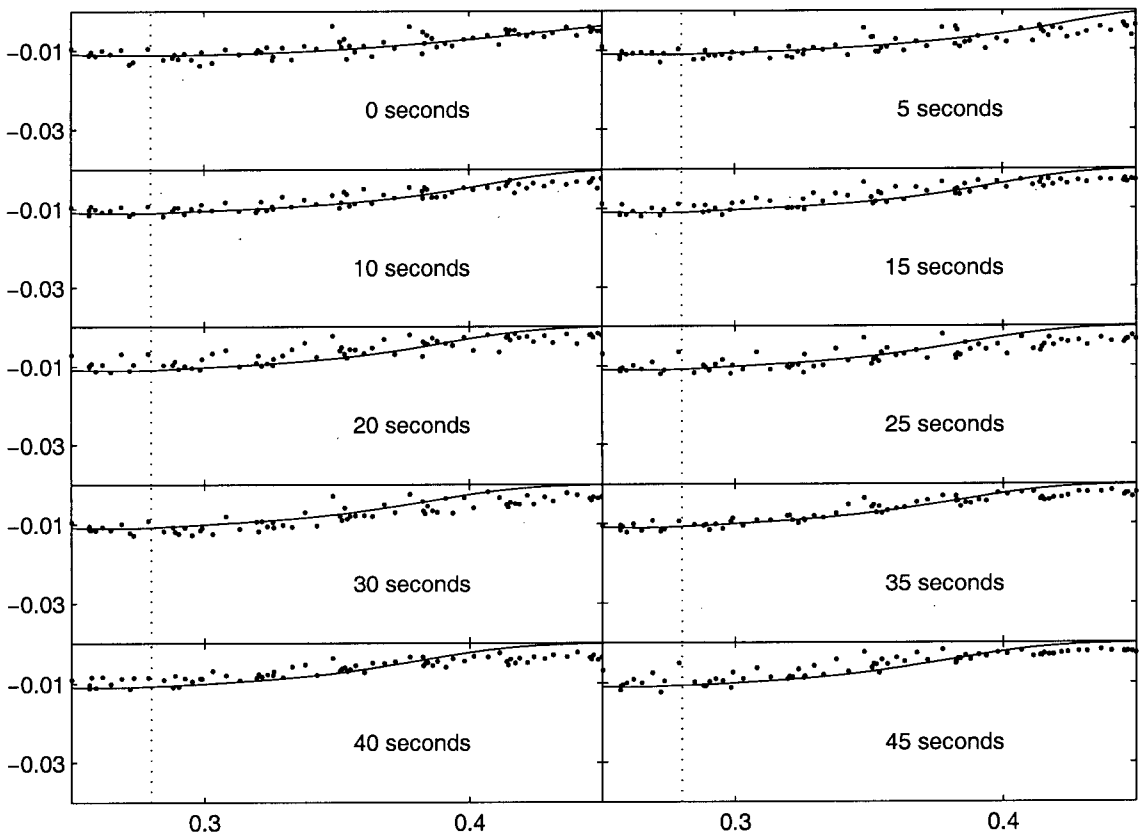

Figure 3.16: Spin-up for trial 7 ($N = 2.2$ s^{-1}, $f = 0.52$ s-1, $\Delta f = 0.09$ s-1) without a canyon, Plots are the same as Figure 3.13. One rotation period is 24.2 seconds.

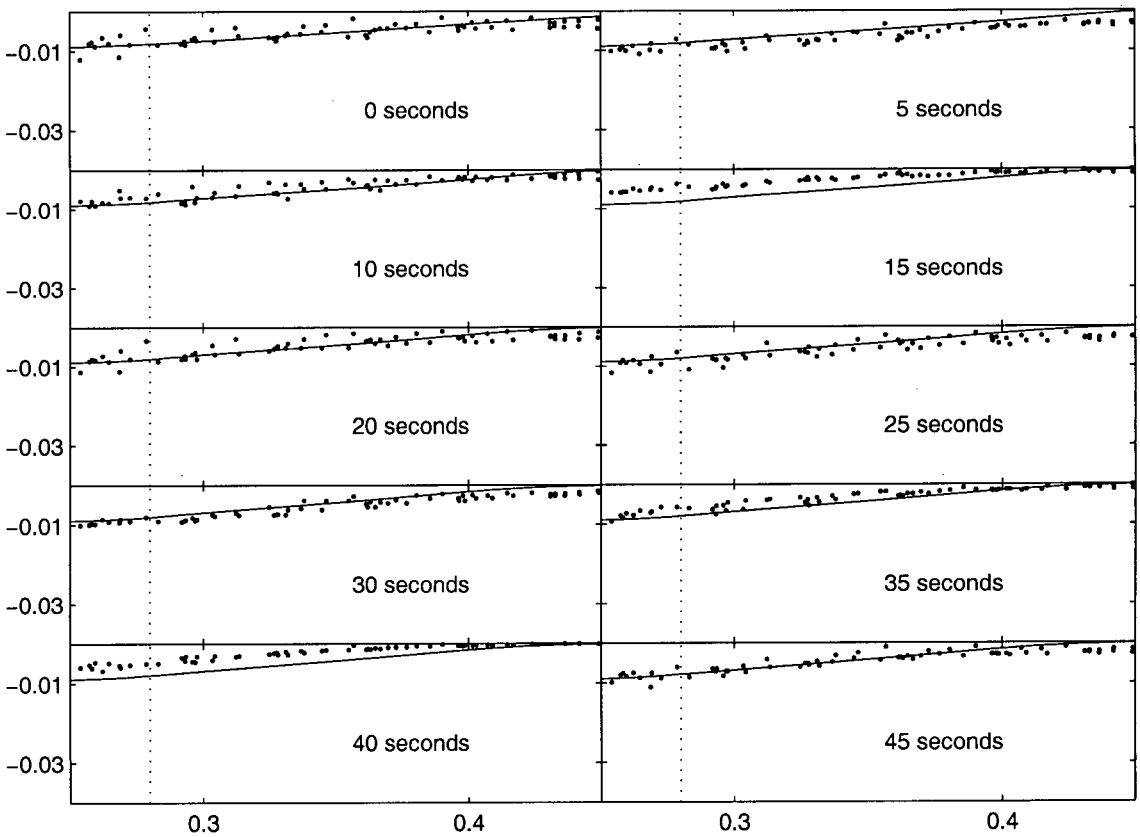

Figure 3.17: Spin-up for trial 8 ($N = 2.2$ s^{-1}, $f = 0.52$ s-1, $\Delta f = 0.06$ s-1) without a canyon, Plots are the same as Figure 3.13. One rotation period is 24.2 seconds.

Chapter 4

Effects of a Submarine Canyon on the Laboratory Flow

4.1 Introduction

In the previous chapter, the problem of how stratified water in the tank with canyon-free topography would respond to a forcing event was studied. The results of that work will now act as the foundations for examining the effect of a canyon on flow evolution. Intuitive expectations are that the presence of any angular-dependence to the tank topography will decrease the spin-up time of the fluid, although to my knowledge, studies examining spin-up over variable topography in a cylindrical tank do not exist, with the exception of one study that examined spin-up over a flat bottom with a radial channel (*Long*, unpublished data).

Studies of flow over topography on the continental shelf have shown that oscillatory or random forcing will result in a mean current (*Holloway*, 1992). This mean current results from unequal forcing effects of the topography in a rotating environment and can be quite strong. As is discussed in Chapter 1, such effects are seen in the flow field after it has passed a submarine canyon. Using the model presented in Chapter 3, the evolution of the flow in the tank with a canyon present can be compared to how the flow would evolve in the absence of a canyon.

Comparing flow evolution of a laboratory trial with and without a canyon present show that the difference in flow evolution is considerable (Figure 4.1). The rate of flow evolution over the continental shelf with a canyon present is much quicker. Careful

examination of the two trials shown in Figure 4.1 shows that their initial conditions (i.e. the velocity distribution across the shelf at the end of forcing) are different due to variations in flow evolution *during* the forcing period.

Experiments performed for this thesis examined only the surface currents in the tank. Quantitatively determining the upwelling flux through a submarine canyon is one of the key questions driving research on currents near submarine canyons. The challenge, then, has been to determine how currents traveling near or through the submarine canyon will affect the flow evolution, and how one can examine the flow evolution to determine the amount of water upwelled through the canyon.

4.2 Qualitative Evidence of Canyon Effects

Before beginning quantitative analysis, it is useful to develop an understanding of how a canyon might affect the flow on the continental shelf. The flow behaviour is easily visualized for a homogeneous fluid in the laboratory. Pathlines can be generated by overlaying images in the flow (Figure 4.2), showing that the canyon effect is large.

At the end of the forcing period (Figure 4.2a), adjustment to the presence of a canyon has begun; a towards-shore deviation in the flow can be seen downstream of the canyon. Over the next 30 seconds the flow evolves further (Figure 4.2b). The location where the flow begins to deviate in the up-canyon direction moves upstream - likely due to the decrease in flow rate past the canyon. It also seems to be getting stronger compared to the flow on the shelf. This could be because the water travelling over the slope spins-up more slowly than the water over the shelf. As a result, when it is advected over the shelfbreak through the canyon, its velocity is larger than the autochthonous water present over the shelf. Hence, the effect of water being carried onto the continental shelf from the continental slope is becoming larger compared to the flow travelling over

the shelf. The apparent absence of particles downstream of the canyon may be due to the advective upwelling causing a surface divergence, although with no visualisation of the currents upstream of the canyon, one cannot be sure. These effects are further emphasized another 30 seconds later (Figure 4.2c). At this stage, the flow on the shelf has halted almost completely, as can be seen downstream of the canyon near the edge of the tank.

The trials that receive quantitative analysis in this chapter are all stratified. As such it is emphasized that the effects seen here are qualitative and meant for visual or conceptual aid. The strong canyon effects on surface flow in a homogeneous fluid will not propagate to the surface in the same manner for a stratified fluid. The effects seen in Figures 4.1 and 4.2 are due to the upwelling component of the flow through the canyon, but they are also due to the drag effects imposed by the canyon on the flow as the two are correlated.

4.3 Drag

When a fluid travels past any solid body, the body will impose a set of forces on the fluid. There will be a tangential stress, which is due to the inertial viscosity of the fluid, and there will be a normal stress. The normal stress is comprised of

- a lift force, which is the component of the total drag force that is normal to the direction of motion;
- an induced drag, which is due to the transfer of kinetic energy between the fluid and the body, and manifests itself as a trail of vortices; and
- a form drag, which is the resultant pressure force parallel to the velocity (but in the opposite direction) after the induced drag has been subtracted (*Batchelor*, 1967).

Upwelling through a canyon is due to inviscid dynamics in the fluid-topography interaction. It follows that the slowing effects seen in Figure 4.1 are almost entirely due non-frictional drag (referred to hereafter simply as drag). It is the stresses normal to the canyon topography but parallel to the flow direction (induced drag and form drag) that will be used to determine upwelling here.

The strong, almost swirling effects seen in the homogeneous case, supply evidence that as the currents travel past the canyon they cross bathymetry contours. This behaviour results in the flow direction not being parallel to the topography, creating drag. As is illustrated in §1.1.1, upwelling in submarine canyons occurs because the sudden changes in topography are strong enough that geostrophy breaks down and the water column experiences vortex tube stretching as it is advected across the bathymetry contours of the canyon. An alternative way to visualize the problem is that as the fluid passes over the canyon, it feels a drag force imposed by the topography which results in upwelling (Figure 4.3). The presence of this drag force, therefore presents a method for considering canyon upwelling in an evolving flow. While this method does not permit one to understand the provinces of flow within a canyon, it does provide a technique for quantitatively determining upwelling through a submarine canyon in the laboratory.

4.3.1 Determining Canyon Drag Contributions To The Evolving Flow

Chapter 3 examines the important properties governing stratified spin-up in the laboratory. The results demonstrate that the important variables are the shear flow in the fluid, which determines the strength of flux into the bottom Ekman layer, as well as the stratification and bottom slope, which determine the rate at which the bottom boundary layer shuts down, eventually invoking diffusive spin-up over a slippery bottom boundary layer.

Using velocity measurements for trials where a canyon is present, it is possible to use

the spin-up model derived and tested in Chapter 3 to determine the effect of a canyon on flow evolution. Velocity measurements were taken from trials with a canyon present and entered as initial conditions into the theoretical "no canyon" model. After one rotation period ($4\pi f$), the model velocities are compared to the measured velocities. If the effect of a canyon were non-existent, then one would expect the model output to agree with the laboratory results. It is already known that the canyon does affect flow evolution (Figure 4.1), and a difference between the model predictions and laboratory measurements is anticipated. This difference is used to calculate the difference in along-shore flux over the shelf, $\Delta\Phi$, as

$$\Delta\Phi(r) = \Delta v(r)h(r), \tag{4.1}$$

where Δv is the difference between the velocity in the laboratory and the model velocity. The difference in flux can be used to calculate the drag imposed by the canyon using Newton's second law of motion, *Force* = *Mass* × *Acceleration*:

$$F = (\rho V)(\Delta v/\Delta t), \tag{4.2}$$

which can be rewritten as

$$F = \frac{\rho 2\pi}{\Delta t}\int_{\text{shelbreak}}^{\text{tank edge}} \Delta\Phi(r) r dr \tag{4.3}$$

where $F\Delta t$ is the impulse imposed on the flow by the canyon in the time Δt, and F is the average force applied by the canyon over that time. Note that the force is calculated for the entire water mass within the radial limits of integration (through the entire angle 2π), rather than simply over the canyon. This domain of integration is chosen because the measured flow evolution is assumed to be representative of the effect of the canyon on the entire shelf, so the force that is measured is one that is effectively applied to the entire mass of water over the shelf. An example of the results obtained by this method is shown in Figure 4.4, except that in the figure, (4.3) has not yet been integrated.

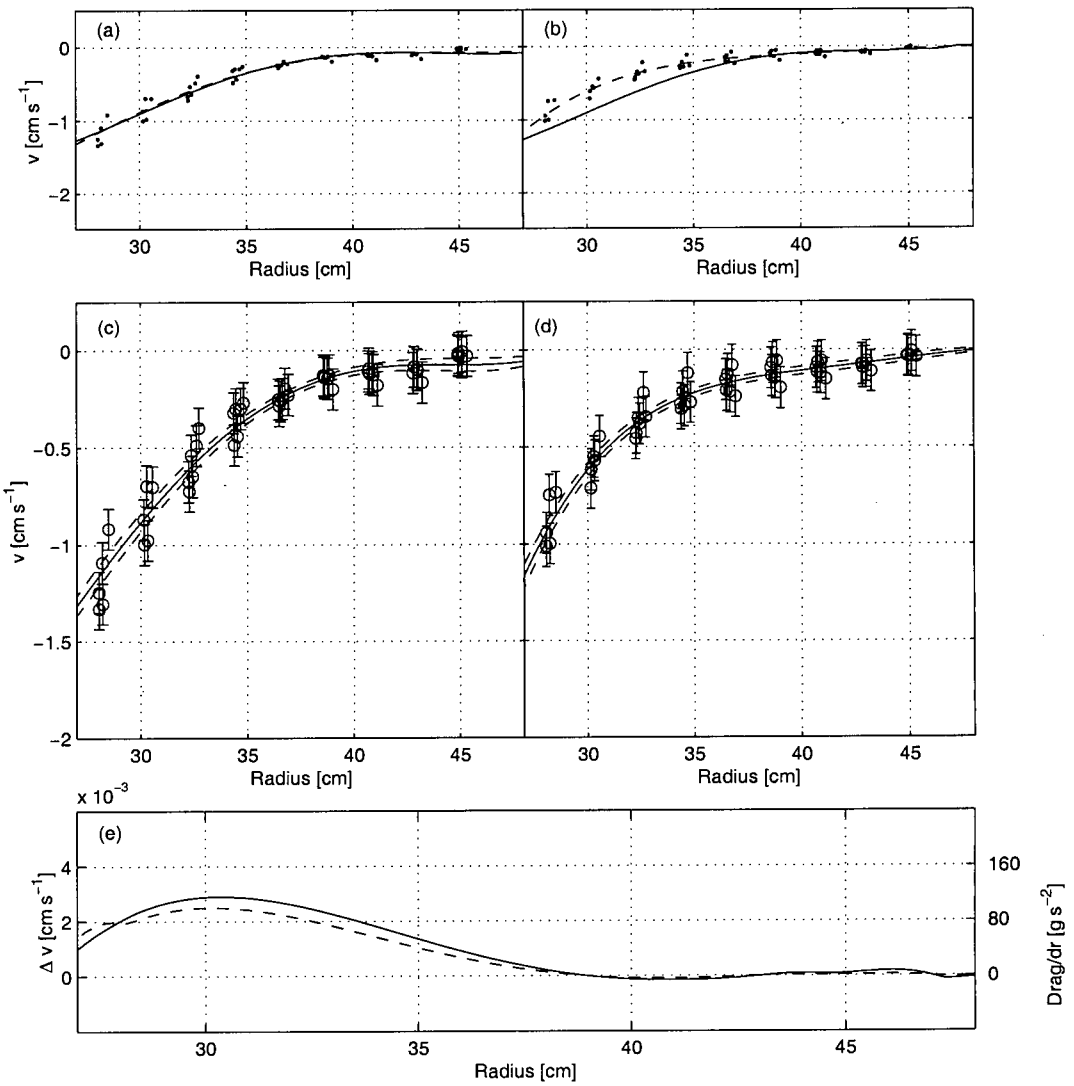

Figure 4.4: Calculation of drag by the canyon from model output. a) Initial conditions of flow (solid line) from laboratory measurements (dots); b) canyon-free expectation of flow evolution (solid line), and actual flow evolution (dashed line) fit to laboratory data (dots); c) points shown in a) with uncertainty and the line fit through the data in a). Dashed lines represent the uncertainty of the fit; d) same as c) except for b); e) difference in velocities given in b) (solid line) and calculated drag from the canyon (dashed line) dr is equal to the radial spacing in the theoretical model.

The uncertainty in the curves shown in Figure 4.4c and d are calculated using the same bootstrap-like method described in §3.3.6. To determine the uncertainty in predicted flow evolution, the three curves in Figure 4.4c (the average curve of best fit and the two "error curves") are then each run through the theoretical model. The outputs of the error bars represent what the horizontal current profile would look like if it started as the error bar. As a result, the uncertainty given by the outputs will not necessarily have a normal distribution and was calculated using the method shown in Figure 4.5.

4.4 Analysis of Results

One can make out a measurable effect of the canyon on spin-up, and this can be expressed as a drag force. Traditionally, a drag force in a non-rotating fluid is be described as

$$F = \rho C_d L_1 L_2 U^2, \tag{4.4}$$

where ρ is the density, C_d is the drag coefficient, L_1 and L_2 are the appropriate lengthscales, and U is the velocity. For the purposes here, ρ is assumed to have the constant value, 1 g cm^{-3} (all units used in this analysis are c.g.i. units). The lengthscales L_1 and L_2 are not determined in this thesis and are combined into a constant, allowing (4.4) to be rewritten as

$$\frac{F}{\rho U_{sb}^2} = AC_d \tag{4.5}$$

where A is an unknown constant with units of cm^2, and U_{sb} is the velocity at the shelfbreak.

The relationship between the drag force and the square of the velocity suggests that there is some variation in C_d between the various trials (Figure 4.6). (The results presented in this section are presented graphically. Raw data for U,N,f and F are compiled into tables and presented in Appendix A.) The stratification (N), shelfbreak velocity

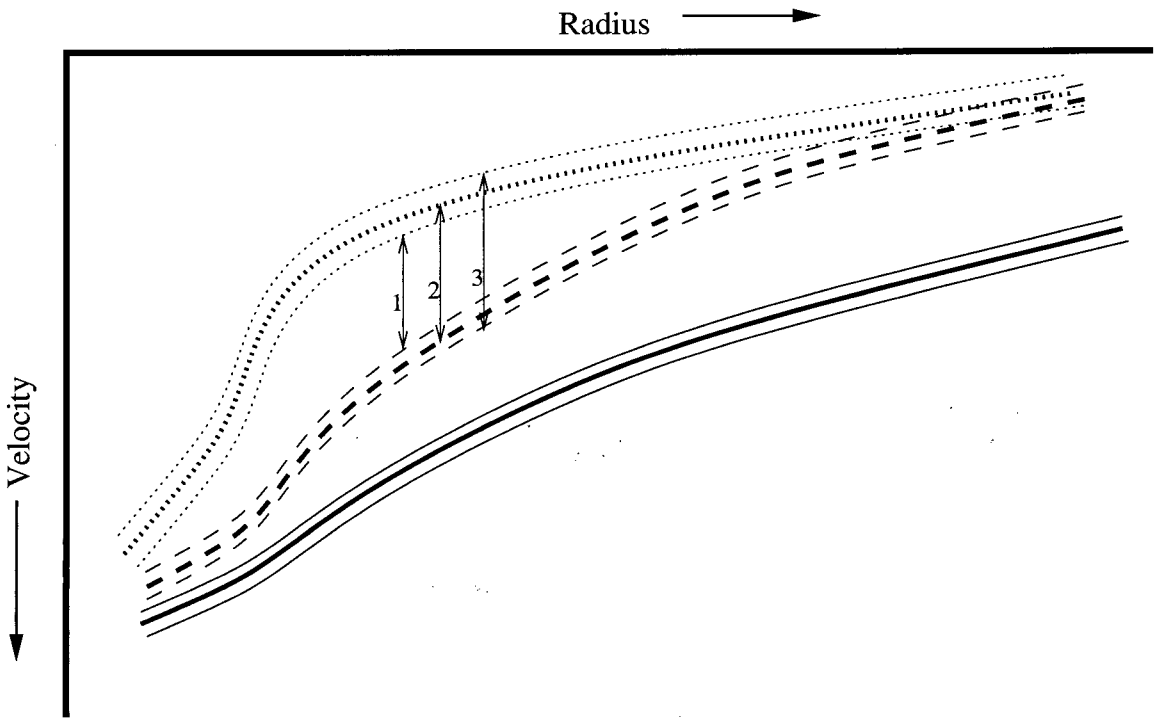

Figure 4.5: Schematic showing the method used for determining errors in flux measurements. The thick solid line represents the initial conditions taken from the laboratory trial. The thick dashed line represents the model predictions for how the flow field shown by the solid line would have evolved in the absence of a canyon. The thick dotted line represents how the flow in the laboratory with a canyon present actually evolved. Thin lines that flank the thicker lines of the same format represent the uncertainty in those measurements. The value for Δv is equal to the distance expressed by line 2. Line 1 and line 3 represent minimum and maximum values, respectively.

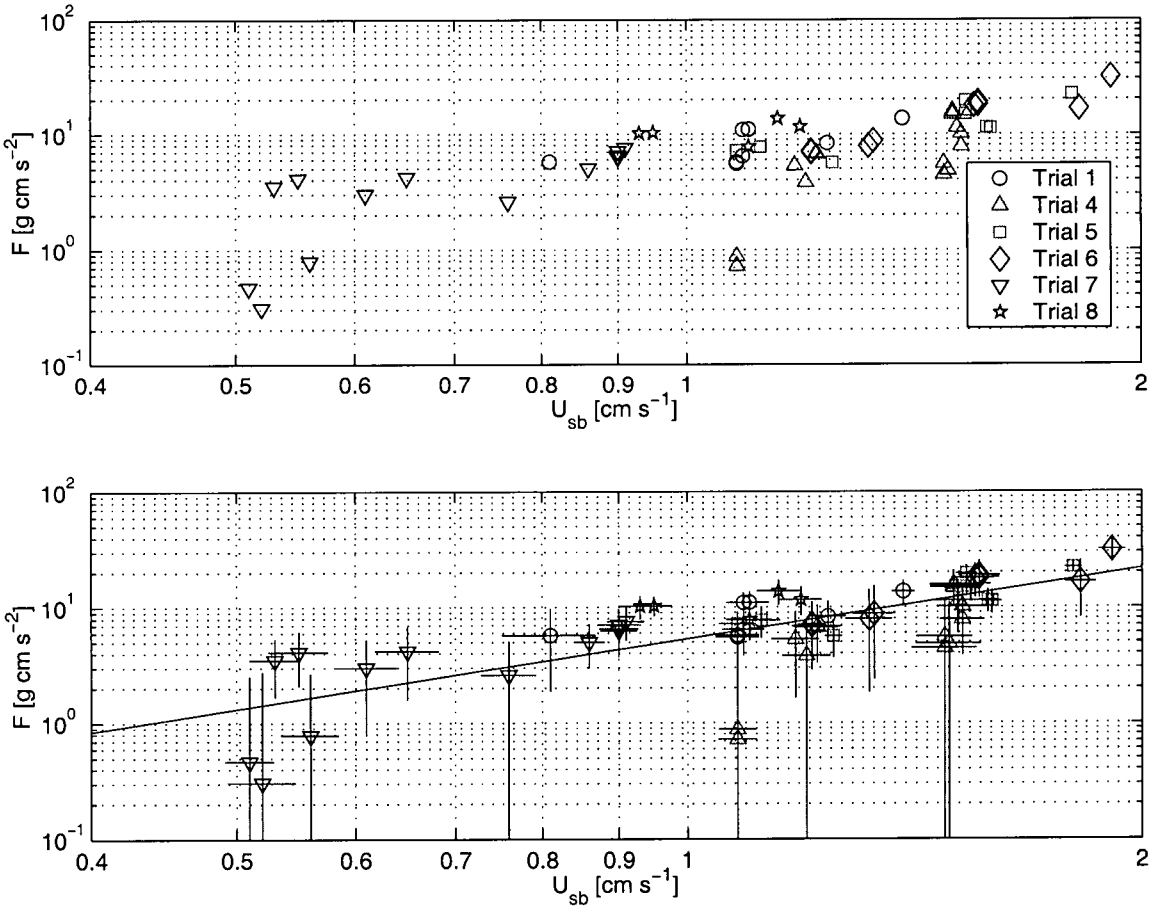

Figure 4.6: Drag forces as a function of the shelfbreak velocity squared are presented for all trials. The data in the top figure are identical to the bottom figure except that error bars are absent in the top figure for clarity. The bottom figure also shows the line of best fit through the data, giving a relationship of $F \propto U^{2.02}$.

(U_{sb}), and rotation rate (f) appear to be important in determining drag effects by the canyon and it is expected that $C_d = C_d(U_{sb}, N, f)$. The relationship between each of these dimensional parameters and $F/(\rho U_{sb}^2)$ is now compared. Although relationships can be found between these variables independently, it will be shown that they must be compared in combination to determine a final relationship.

4.4.1 Shelfbreak Velocity

The shelfbreak velocity is expected to be one of the key parameters governing the drag imposed by the canyon. The faster the fluid travels, the more it will deviate from a geostrophic balance, resulting in a stronger deviation of the current paths from the isobaths. Perhaps it is surprising, then, that the results shown in Figure 4.6 give no real dependence upon velocity past U_{sb}^2.

4.4.2 Stratification

Stratification will affect the canyon spin-up because only water that is lifted out of the canyon and onto the shelf will contribute to the drag felt by the water over the continental shelf. If the stratification is increased, then a higher amount potential energy must be gained by a fluid parcel travelling up through the canyon from a given depth. If the stratification continues to increase, a time will arrive when fluid particles originating from a given depth will not reach the top of the canyon and therefore will not affect the measured drag at the surface. Examination of the relationship between stratification (N) and drag suggests that the drag is related to the stratification as $N^{-0.83}$ (Figure 4.7).

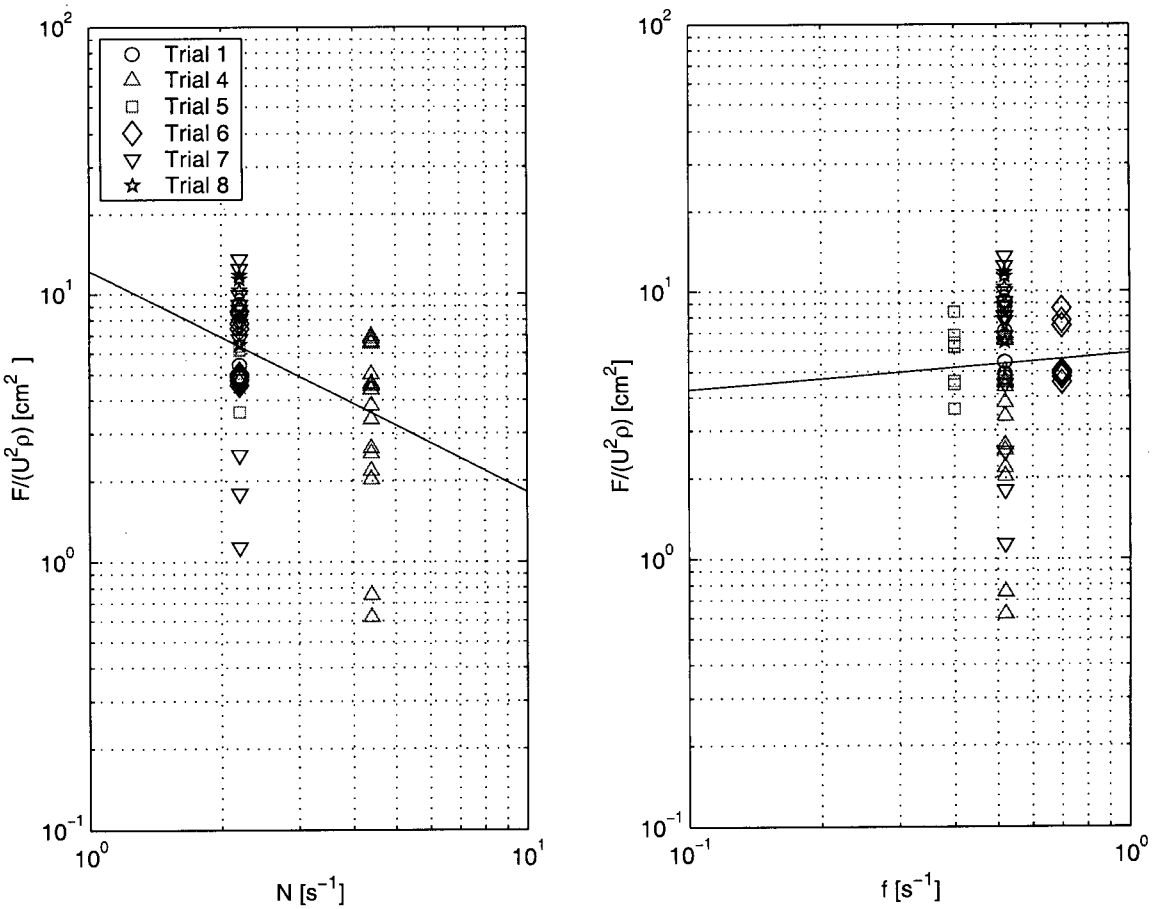

Figure 4.7: Left: the relationship between N and drag, showing data from all trials being compared. A line of best fit to the data provides the relationship $F \propto N^{-0.83}$. Right: the relationship between f and drag, showing data from all trials being compared. The line of best fit gives the relationship $F \propto f^{0.14}$.

4.4.3 Rate of Rotation

Not including its contribution to the Rossby number, f is expected to play a minor role, if any, in the drag force imposed by the canyon. This is because rotational effects should not affect the magnitude of the drag against the fluid once it has left the bathymetry contours and entered the canyon. There apparently is some other dependence on f as its exponent correlates positively with $F/(\rho U_{sb}^2)$. (Figure 4.7)

4.4.4 Combination of Dimensional Parameters

The result determined from the independent relations of U_{sb}, N and f to $F/(\rho U_{sb}^2)$ does not produce a dimensionally feasible solution. Using these results would give $F/(\rho U_{sb}^2 A) = f^{0.14} N^{-0.83} U_{sb}^{0.02}$ which gives C_d the approximate dimensions of $\mathrm{s}^{-0.7}$. This is clearly incorrect, as C_d should be dimensionless. It is likely that the variations of each of these individual parameters is large enough that they cannot be solved individually and must be solved together as a set, i.e.:

$$\frac{F}{\rho U_{sb}^2} = A f^k N^m U_{sb}^n \tag{4.6}$$

or

$$\log(F) - 2\log(U_{sb}) = \log(A_r) + k\log f + m\log N + n\log U_{sb} \tag{4.7}$$

where $A_r = A\rho$. This equation can be solved using a least squares fit which gives $F/(\rho U_{sb}^2) = A f^{-0.01} N^{-0.96} U_{sb}^{0.36}$. Unfortunately, this solution does not match the required dimensions of the problem either. Given the difficulty in scaling F exactly (or nearly exactly) with dimensional coordinates, it makes sense to attempt to force a non-dimensional nature upon C_d by scaling in non-dimensional space.

4.4.5 Non-Dimensional Parameterization of C_d

The dimensionless parameters that can be used to scale the flow are the Rossby number, the Froude number and the Burger number. If it is assumed that $C_d = Ro^k Fr^m Br^n$ then (4.5) can be rewritten as

$$\log(F) - 2\log(U_{sb}) = \log(A_r) + k\log(Ro) + m\log(Fr) + n\log(Br). \tag{4.8}$$

The solution of this problem by a least squares estimate inverts a near-singular matrix suggesting that the choice of scaling is probably poor. The solution to (4.8) is found by rewriting it in matrix form as $F = PQ$, where P are the parameters (1, $\log(Ro)$, $\log(Fr)$ and $\log(Br)$) and Q are the exponents. The values for Q are determined as $Q = (P'P)^{-1}P'F$. To test the validity of this solution for (4.8), the columns of the P were rearranged. This rearrangement resulted in a different answer for Q, suggesting that the choice of scaling was bad, indeed.

Examination of the non-dimensional parameters identifies the problem in the choice of scaling to be $Br = S_c(Ro/Fr)$, where S_c is a constant that is dependent on the spatial scalings in these parameters. Regardless of which of these three parameters is dropped, the final outcome is the same. If the Burger number is dropped then the least-squares problem solves

$$\log(F) - 2\log(U_{sb}) = \log(A_r) + k\log(Ro) + m\log(Fr). \tag{4.9}$$

Error in the approximation is made using the bootstrap method and the predicted values are $\log A = 28\pm14$, $k = -0.47\pm0.27$, and $m = 0.86\pm0.24$. Using these values for A,m and n, (4.9) predicts the behaviour of the drag (Figure 4.8). Recalling that $Ro = U_{sb}/(f\mathcal{R})$ and $Fr = U_{sb}/(NH)$, C_d can be written as

$$C_d = \frac{\mathcal{R}^{0.47\pm0.25}}{H^{0.86\pm0.25}} \frac{U^{0.49\pm0.35} f^{0.47\pm0.25}}{N^{0.86\pm0.25}}. \tag{4.10}$$

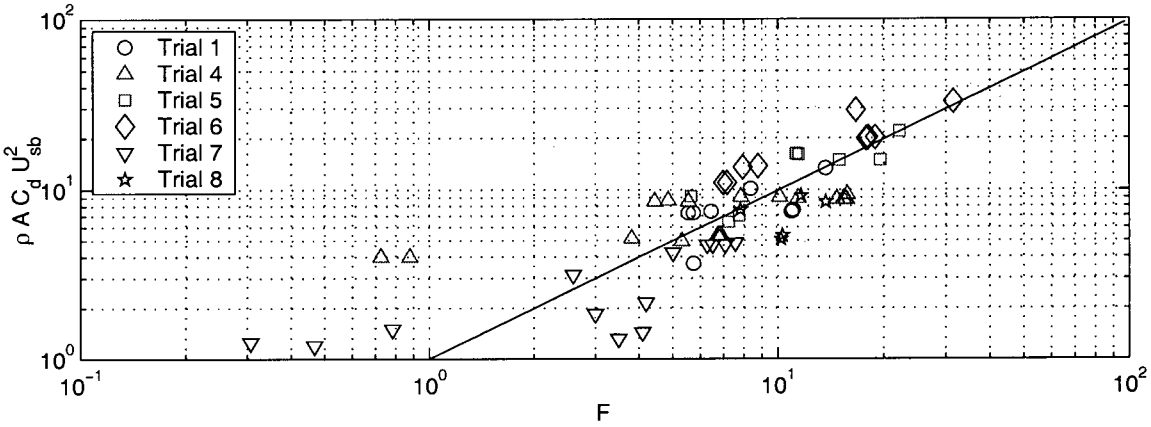

Figure 4.8: Relationship between drag, velocity, Rossby number and Froude number, based on the least squares solution to (4.8). Data are presented on a logarithmic scale. If the data fit the scaling proposed perfectly, they would lie on a straight line with a slope of 1. The line placed present in the figure has a slope of 1. It was not fit to the data but is meant to guide the eye along the correct aspect ratio.

The drag induced by the canyon is therefore

$$F = \rho(28\text{cm}^2 \pm 14\text{cm}^2)\frac{L^{0.47\pm0.25}}{H^{0.86\pm0.25}}\frac{U^{2.49\pm0.35}f^{0.47\pm0.25}}{N^{0.86\pm0.25}}, \tag{4.11}$$

or

$$F \approx \rho(30\text{cm}^2)\frac{L^{0.5}}{H}\frac{U^{2.5}f^{0.5}}{N} \tag{4.12}$$

The upwelling velocity can be determined from this force, as is expressed schematically in Figure 4.3:

$$v_{up} = \frac{F}{fV\rho} \tag{4.13}$$

where v_{up} is the average cross-shelfbreak velocity imposed by the canyon and V is the volume of water affected by the force. In the laboratory, the upwelling flux can be calculated as

$$\Phi_{up} = 2\pi r_{sb} h_{sb} v_{up}, \tag{4.14}$$

where Φ_{up} is the cross-shelfbreak flux due to the canyon and $2\pi r_{sb} h_{sb}$ is the area of the cylindrical wall of water directly above the shelfbreak in the tank. Based on laboratory data, the upwelling flux in the tank is equal to

$$\Phi_{up} \approx \frac{\mathrm{cm}^2\mathrm{s}}{7.3\mathrm{g}} F. \tag{4.15}$$

4.5 Case Study: Predicting the Upwelling Flux Through Astoria Canyon

Taking the findings of this study, it is possible to make predictions for upwelling in coastal submarine canyons. Since most of the relevant information necessary to make this prediction is already in Table 2.1 for Astoria canyon, it will be used as the example. Typical scales for Astoria canyon are $U = 20\mathrm{cm\ s}^{-1}$, $N = 7.5 \times 10^{-3}\mathrm{s}^{-1}$, $f = 10^{-4}\mathrm{s}^{-1}$, $H = 150\mathrm{m}$, $L = 22\mathrm{km}$, $Z = 60\mathrm{m}$, $W_{sb} = 16\mathrm{km}$ and $\mathcal{R} = 4.5\mathrm{km}$, where Z is the depth below the canyon head from which the deepest upwelled water originates as defined by *Allen and Hickey* (in prep.). If it is assumed that the scales of A increase by $O(10^6)$ (corresponding to a change in spatial scales from cm^2 to km^2 – see (4.5)), then the drag induced by Astoria canyon will be approximately 3×10^8 N. If the volume of Astoria canyon is approximately $LW_{sb}Z$ and the area through which the flux enters is ZW_{sb}, then the upwelling flux for Astoria canyon is

$$\Phi_{up} = \frac{F}{fL\rho} \tag{4.16}$$

which is $1.3 \times 10^5 \mathrm{m}^3\mathrm{s}^{-1}$.

4.6 Summary

The flow evolution of laboratory spin-up experiments with a canyon present were compared to theoretical expectations for the spin-up in the absence of a canyon. The theoretical model used velocity measurements from the laboratory as initial conditions

and laboratory data were compared to model output one tank rotation period later. The differences in velocity were used to determine the drag force imposed on the fluid by the canyon. Examining the relationships held between the form drag and the appropriate non-dimensional parameters suggests that the drag felt by the canyon will adhere to the relationship

$$F \propto \frac{U^{5/2} f^{1/2}}{N}.$$

The upwelling flux onto the shelfbreak due to the canyon is determined as $\Phi_{up} \propto F/f$, or

$$\Phi_{up} \propto \frac{U^{5/2}}{N f^{1/2}}.$$

Analysis of these results findings for Astoria canyon suggests that the upwelling flux through Astoria upwelling favourable conditions is $O(10^5 \mathrm{m}^3\mathrm{s}^{-1})$.

Chapter 5

Discussion and Conclusions

The goal of this thesis was to determine how water and current properties upstream of a submarine canyon will affect the amount of upwelling through it. The problem was solved by studying how the presence of a submarine canyon affects the spin-up rate of a fluid in the laboratory, and using the flow evolution to determine drag induced by the canyon. This study is the first where the drag is measured through analysis of the spin-up problem. The measured drag can be used to estimate upwelling through the submarine canyon.

5.1 Laboratory Methods

Originally, eight trials were intended to be run and compared. In Trial 2, the fluid was homogeneous and the results were necessary to verift the Ekman suction model presented in Chapter 3. While results for Trial 2 with a canyon present were used for qualitative visualisation of canyon effects on flow over the shelf, predictions of the ensuing form drag were not made. Results for Trial 3 with a canyon present were unfortunately lost and could not be analyzed.

Laboratory measurements made in this thesis were contaminated by an oscillation in the velocity due to the fact that the axis of rotation was not perfectly normal to the vertical. Although attempts were made to level the tank, it seems that the accuracy required was beyond the methods used and made it difficult to examine the flow late in time. Nevertheless, quantitative predictions of how the canyon affects the flow were still

found and match well with intuitive expectations of the flow behaviour.

The use of PIV methods worked as an excellent tool for flow measurements. This project reintroduced the methods to the laboratory, and although the error in measurements still allowed meaningful results, the uncertainties could likely be reduced further.

5.2 Laboratory Spin-up With and Without a Canyon

Analysis of the momentum equations for the boundary layer of a homogeneous fluid on a slope provides three important observations:

- the thickness of the boundary layer will increase as $(\cos\gamma)^{-1/2}$;
- the strength of vortex stretching in the interior due to Ekman suction will remain a constant of the flow vorticity;
- Ekman suction will have a horizontal component proportional $\sin\gamma$.

These expectations are consistent with laboratory observations.

The behaviour of the bottom boundary layer in a stratified, rotating fluid over a shallow slope is described by *MacCready and Rhines*(1991). They predict the boundary layer to shutdown on a timescale $\tau = (1/\sigma + S)/[(1+S)S^2 f\cos\gamma]$, after which diffusion over a slippery bottom boundary layer will govern the spin-up process. In order to consider the effects of horizontal diffusion in regions of high horizontal shear, the diffusion solution proposed by *MacCready and Rhines* (1991) is modified slightly. This theory is used to successfully replicate the spin-up results for a stratified fluid in the laboratory when a canyon is not present.

The introduction of a submarine canyon to the laboratory topography changes the spin-up regime in the laboratory. Using the theory mentioned above, comparisons of the flow evolution with and without a canyon provided a measurable effect of its presence,

from which the force (or drag) imposed on the fluid by the canyon was approximated. The experiment was repeated for various values of f, U and N and an empirical relationship between the drag force and these parameters was found. Analyzing each of these parameters individually would give a possible scaling of $F \propto U^2 N^{-1}$, but this scaling is dimensionally incorrect. Scaling by U^2 and the non-dimensional numbers Fr and Ro gives a dimensionally correct scaling of $F \propto U^{5/2} f^{-1/2} N^{-1}$.

The relationship between the drag force and the upwelling velocity is quite simple, which makes it possible to predict the relationship of the upwelling flux through the canyon to the above parameters as

$$\Phi_{up} \propto \frac{U^{5/2}}{N f^{1/2}}.$$

5.3 Scatter in Data Measurements

The data presented in Chapter 4 displays a large amount of scatter, which is most likely because the velocity used for drag calculations is derived from the shelfbreak region, which falsely assumes that the flow over the length of the canyon is constant. While this assumption seems correct in the real ocean, it does not hold in the laboratory. By the end of the forcing period, the velocity at the head of the canyon is about 30% of what it is at the shelfbreak (Figure 4.1b). While a large portion of the drag experienced by the flow will be from water whose source is near the shelfbreak, some drag is likely from water closer to the head of the canyon.

Also, high frequency changes in the velocity (seen in Figure 4.1) could cause values of the predicted drag to be higher or lower, depending on if the data were sampled in a high or low point in these bumps (either in the initial conditions or in the final measurements). This occurrence would alter the expected drag value considerably. These high-frequency oscillations are radially and azimuthally continuous, suggesting that it is not an artifact

of the sampling method, such as windowing or biasing in the PIV process. Instead, it is likely that they are due to inconsistencies in table rotation, as they appear to be of the same magnitude as the precision of the instruments that control the rotation rate of the table.

Despite these uncertainties, the signal of the upwelled water is strong and consistent enough that a believable relationship is still found. A scaling analysis of the flux through a laboratory canyon being developed by *Allen and Hickey* (in prep.) quantify the amount of water travelling through a canyon, ϕ, as

$$\phi = W_{sb} Z U_{sb} \mathcal{F} H, \tag{5.1}$$

where $Z = (\sqrt{f U_{sb} L \mathcal{F}})/N$, $\mathcal{F} = 2(Ro + G - RoG)/3$, $G = -(1./Ro - \sqrt{4 + 1/Ro^2})/2$, $H = \sqrt{1/(4R_w^2) + 1/R_w} - 1/(2R_w)$ and $R_w = U_{sb}\mathcal{F}/(fW_{sb})$. W_{sb} is the distance across the canyon at the shelfbreak, Z is the maximum depth from which water can enter the canyon and exit onto the shelf and $U_{sb}\mathcal{F}H$ is the amount of water entering the canyon at its head. The findings presented in Chapter 4 support this theory (Figure 5.1) and a linear relationship between them appears to be present.

5.4 Implications of Findings

In §4.5, the findings of this study were applied to Astoria canyon to determine its upwelling flux as $1.3 \times 10^5 \mathrm{m}^3\mathrm{s}^{-1}$. To put this value in context, it is compared to a prediction of wind-forced upwelling at the shelfbreak. Assuming an Ekman balance between the wind stress and the ocean currents, the wind stress, $\vec{\tau}$, will create a surface flux

$$u = \frac{\tau_y}{\rho f} \tag{5.2}$$

$$v = -\frac{\tau_x}{\rho f} \tag{5.3}$$

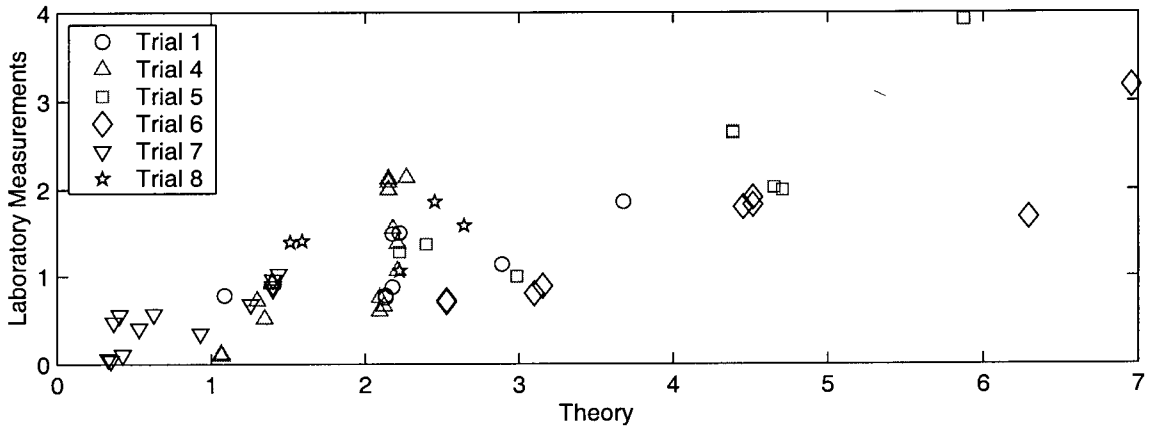

Figure 5.1: Comparing upwelling measurements from the laboratory with those predicted by the theory described by *Allen and Hickey*(in prep.) (ϕ). Both are in units of cm^3s^{-1}. A line of best fit through the origin gives a slope of 0.3 $\pm$ 0.02.

where the axes define a right-handed system relative to the coast with y increasing in the offshore direction, f is the Coriolis frequency, ρ is the density, u and v are the velocities in the x and y direction, respectively, and τ_x and τ_y are the wind stress in the x and y directions, respectively.

Lentz (1992) found that the mean wind stress over the Oregon shelf from July 5 to August 28, 1973 was parallel to the coast with $\vec{\tau} = \tau_x$ = -0.45 dyn cm^{-2}, where 1 dyn = 10^{-5}N. For a fluid density of 1000 kg m^{-3} the offshore flux of surface water due to the wind will be 0.45 m^3s^{-1} for each meter along the shelfbreak. By continuity, there must be a towards-shore return flow of equal magnitude. Astoria canyon has width of 1.6×10^4m. A region of shelfbreak equal to the shelfbreak width of Astoria canyon will therefore have a towards shore flux of $7.2 \times 10^3 m^3s^{-1}$, suggesting that the flux through Astoria canyon is almost 20 times larger than that over a section of shelfbreak of equal width.

5.5 Future Work

The spatial and temporal features of a given canyon are unique. The magnitude of difference in upwelling determined between Astoria canyon and an appropriate length of shelfbreak is not identical for other canyons. A project gathering the dimensional parameters of all the canyons off the west coast of North America has already begun. These data will be used with the necessary flow and water property information to determine the upwelling flux of water through each of these submarine canyons.

The laboratory work is to be followed by a similar set of experiments as those performed in this thesis except that their goal will be to determine the role of a canyon in down-welling favourable flow, which is characteristic of the winter season off of the coast of British Columbia. This may prove to be quite challenging due to the behaviour of boundary layers on a slope in a stratified fluid. In order to force downwelling currents in the laboratory, one must decrease the rotation rate. This will add cyclonic vorticity to the water in the tank and the water in the boundary layer will travel radially inward. As it travels downslope, however, the water in the boundary layer will be advected a region of higher density, causing it to become unstable. Instabilities in boundary layers travelling downslope have will have mixing efficiencies an order of magnitude higher than those travelling upslope (*Condie*, 1999). A second proposed laboratory study, which may help to explain the scatter in the drag-velocity relationship, would develop a three-dimensional map of submarine canyon flow.

Bibliography

Allen, S. (1996). Topographically generated, subinertial flows within a finite length canyon. *J. Phys. Oceanogr.*, 26(8):1608–1632.

Allen, S. (2000). On subinertial flow in submarine canyons: Effect of geometry. *J. Geophys. Res.*, 105:1285–1297.

Allen, S., Dinniman, M., Gorby, D., Klinck, J., Hewett, T., and She, J. (submitted). Numerical and physical modelling: A comparison over steep topography. *J. Geophys. Res.*

Allen, S. and Hickey, B. (in prep.). Dynamics of advection-driven upwelling over a submarine canyon.

Allen, S. E., Vindeirinho, C., Thomson, R. E., Foreman, M. G., and Mackas, D. L. (2001). Physical and biological processes over a submarine canyon during an upwelling event. *Can. J. Fish. Sci.*, 58(4):671–684.

Batchelor, G. (1967). *An Introduction to Fluid Dynamics.* Cambridge University Press, Cambridge, 615 pp.

Benton, E. (1973). Nonlinear hydrodynamic and hydromagnetic spin-up driven by ekman-hartmann boundary layers. *J. Fluid Mech.*, 57:337–360.

Benton, E. and Clark, Jr., A. (1974). Spin-up. *Ann. Rev. Fluid Mech.*, 6:257–280.

Boyer, D. L. and Davies, P. A. (2000). Laboratory studies of orographic effects in rotating and stratified flows. *Ann. Rev. Fluid Mech.*, 32:165–202.

Charney, J. and Eliassen, A. (1949). A numerical method for predicting the perturbations of the middle latitude westerlies. *Tellus*, 1:38–54.

Chen, X. and Allen, S. E. (1996). The influence of canyons on shelf currents: A theoretical study. *J. Geophys. Res.*, 101:18043–18059.

Condie, S. A. (1999). Ocean boundary mixing during Ekman layer arrest. *J. Phys. Oceanogr.*, 29:2993–3001.

Durrieau de Madron, X. (1994). Hydrography and nephaloid structure in the Grand-Rhone canyon. *Contin. Shelf Res.*, 14:457–477.

Ekman, V. W. (1905). On the influence of the earth's rotation on ocean currents. *Arkiv. Matem., Ast. Fysik*, 2:1–52.

Foreman, M. G. G. and Thomson, R. E. (1997). Three-dimensional model simulations of tides and buoyancy currents along the West Coast of Vancouver Island. *J. Phys. Oceanogr.*, 27:1300–1325.

Freeland, H. and Denman, K. (1982). A topographically controlled upwelling center off Vancouver Island. *J. Marine Res.*, 40:1069–1093.

Greenspan, H. (1964). On the transient motion of a contained rotating fluid. *J. Fluid Mech.*, 21:673–696.

Greenspan, H. (1965). On the general theory of contained rotating fluid motions. *J. Fluid Mech.*, 22:449–462.

Greenspan, H. (1968). *The Theory of Rotating Flows.* Cambridge University Press, 327pp., Cambridge.

Greenspan, H. and Howard, L. (1963). On a time-dependent motion of a rotating fluid. *J. Fluid Mech.*, 17:385–404.

Han, G., Hansan, D., and Galt, J. (1980). Steady-state diagnostic model of the New York Bight. *J. Phys. Oceanogr.*, 10:1998–2020.

Hart, J. (2000). A note on nonlinear corrections to the Ekman layer pumping velocity. *Physics of Fluids*, 12(1):131–135.

Hewett, A. (1998). Laboratory simulation of a geophysical flow past a submarine canyon. Honour's thesis at the University of British Columbia.

Hickey, B. (1997). The response of a narrow canyon to strong wind forcing. *J. Phys. Oceanogr.*, 27(5):697–726.

Hickey, B. M. (1995). Coastal submarine canyons. In Muller, P. and Henderson, D., editors, *'Aha Huliko'a Hawaiian Winter Workshop on topographic effec ts in the ocean*, pages 95–110, University of Hawaii at Manoa. SOEST Special Publication.

Hickey, B. M., Baker, E., and Kachel, N. (1986). Suspended particle movement in and around Quinault submarine canyon. *Marine Geol.*, 71:35–83.

Holloway, G. (1992). Representing topographic stress for large-scale ocean models. *J. Phys. Oceanogr.*, 22:1033–1046.

Holton, J. R. (1965). The influence of viscous boundary layers on transient motions in a stratified fluid: part I. *J. Atm. Sci.*, 22:402–411.

Holton, J. R. (1967). The diurnal boundary layer wind oscillation above sloping terrain. *Tellus*, 19:199–205.

Hsueh, Y. (1969). Buoyant Ekman layer. *Phys. Fluids*, 12:1757–1762.

Hutchins, D. and Bruland, K. (1998). Iron-limited diatom growth and Si:N uptake ratios in a coastal region. *Nature*, 393:561–564.

Klinck, J. (1988). The influence of a narrow transverse canyon on an initially geostrophic flow. *J. Geophys. Res.*, 93:509–515.

Klinck, J. (1989). Geostrophic adjustment over submarine canyons. *J. Geophys. Res.*, 94:6133–6144.

Klinck, J. (1995). Circulation near submarine canyons: a modelling study. *J. Geophys. Res.*, 101:1211–1223.

Lentz, S. J. (1992). The surface boundary layer in coastal upwelling regions. *J. Phys. Oceanogr.*, 122:1517–1539.

Linden, P. and van Heifst, G. (1984). Two-layer spin-up and frontogenesis. *J. Fluid Mech.*, 143:69–94.

MacCready, P. and Rhines, P. B. (1991). Buoyant inhibition of Ekman transport on a slope and its effect on stratified spin-up. *J. Fluid Mech.*, 223:631–661.

MacCready, P. and Rhines, P. B. (1993). Slippery bottom boundary layers on a slope. *J. Phys. Oceanogr.*, 23:5–22.

Mackas, D. L., Kieser, R., Saunders, M., Yelland, D. R., Brown, R. M., and Moore, D. F. (1997). Aggregation of euphasics and Pacific Hake (*merluccius productus*) along the outer continental shelf off Vancouver Island. *Can. J. Aquat. Sci.*, 57:2080–2096.

O'Donnell, J. and Linden, P. (1991). Free-surface effects on the spin-up of fluid in a rotating cylinder. *J. Fluid Mech.*, 232:439–453.

Osler, G. (1965). Density gradients. *Scientific American*, 213:70–76.

Pedlosky, J. (1987). *Geophysical Fluid Dynamics, 2^{nd} Ed.* Springer-Verlag, Ann Arbor, USA, 710pp.

Pérrene, N., Verron, J., Renouard, D., Boyer, D., and Zhang, X. (1997). Rectified barotropic flow over a submarine canyon. *J. Phys. Oceanogr.*, 27(9):1868–1893.

Press, W., Flannery, B., Teukolsky, S., and Vetterling (1986). *Numerical Receipes: the Art of Scientific Computing.* Cambridge University Press, Cambridge, 818pp.

Raffel, M., Willert, C., and Kompenhans, J. (1998). *Particle Image Velocimetry: A Practical Guide.* Springer-Verlag, Berlin, Germany.

Sveen, J. (2000). *An introduction to MatPIV v.1.4.* University of Oslo, Norway. pp. 18.

Thomson, R. (1981). *Oceanography of the British Columbia Coast.* Department of Fisheries and Oceans.

Thorpe, S. (1987). Current and temperature variability on the continental slope. *Phil. Trans. Roy. Soc. Lon.*, A323:471–517.

Thurman, H. (1994). *Introductory Oceanography.* MacMillan Publishing Company, New York, 550pp.

van de Konijnenberg, J. and van Heijst, G. (1995a). Nonlinear spin-up of a circular cylinder. *Phys. Fluids*, 7:2989–2999.

van de Konijnenberg, J., Wessels, T., and ven Heijst, G. (1996). Spin-up in a circular tank with a radial barrier. *Phys. Fluids*, 8(8):2048–2059.

van de Konijnenberg, J. A. and van Heijst, G. (1995b). Nonlinear spin-up in a circular cylinder. *Phys. Fluids*, 7(12):2989–2999.

Vindeirinho, C. (1998). Water properties, currents and zooplankton distribution over a submarine canyon under upwelling favourable conditions. Master's thesis, University of British Columbia, Vancouver, B.C., Canada.

Weatherly, G. and Marin, P. (1978). On the structure and dynamics of the ocean bottom boundary layer. *J. Phys. Oceanogr.*, 8:557–570.

Wedemeyer, E. (1964). The unsteady flow within a cylinder. *J. Fluid Mech.*, 20:383–99.

Willert, C. (1996). The fully digital evaluation of photographic PIV recordings. *Appl. Sci. Res.*, 56:79–102.

Appendix A

Canyon Flux Measurements

The tables presented in this appendix give the raw data that are used in for the production of figures in Chapter 4. The value for the shelfbreak velocity, U_{sb} is calculated as the mean surface velocity between 27 and 30 cm.

Time [s]	U_{sb} [cm s^{-1}]	Drag	[g cm s^{-2}]	Φ_{up} [cm^3 s^{-1}]
15.8	-1.20 +0.044/-0.044	3.81	+4.032/-3.893	0.52 +0.549/-0.530
25.6	-1.10 +0.031/-0.031	11.04	+2.515/-2.469	1.50 +0.342/-0.336
26.4	-1.50 +0.052/-0.052	14.73	+5.075/-4.829	2.00 +0.691/-0.657
27.0	-1.09 +0.028/-0.028	10.93	+2.463/-2.416	1.49 +0.335/-0.329
30.6	-1.09 +0.035/-0.035	6.44	+2.669/-2.616	0.88 +0.363/-0.356
31.2	-1.50 +0.053/-0.053	15.61	+5.162/-4.919	2.12 +0.702/-0.669
31.8	-1.08 +0.036/-0.036	5.53	+2.814/-2.761	0.75 +0.383/-0.376
35.4	-1.50 +0.049/-0.049	15.64	+5.074/-4.822	2.13 +0.690/-0.656
41.6	-1.50 +0.052/-0.052	15.34	+5.487/-5.216	2.09 +0.747/-0.710

Table A.1: Drag and upwelling flux predictions for trial 1 ($f = 0.52$ s^{-1}, $N = 2.2$ s^{-1}).

Time [s]	U_{sb} [cm s^{-1}]	Drag	[g cm s^{-2}]	Φ_{up} [cm^3 s^{-1}]
10.8	-1.08 +0.036/-0.036	5.73	+2.737/-2.685	0.78 +0.372/-0.365
11.6	-1.09 +0.028/-0.028	10.93	+2.463/-2.416	1.49 +0.335/-0.329
13.2	-1.08 +0.036/-0.036	5.53	+2.814/-2.761	0.75 +0.383/-0.376
13.4	-1.50 +0.053/-0.053	15.61	+5.162/-4.919	2.12 +0.702/-0.669
13.6	-1.10 +0.031/-0.031	11.04	+2.515/-2.469	1.50 +0.342/-0.336
14.4	-1.58 +0.020/-0.020	17.95	+3.302/-3.141	2.44 +0.449/-0.427
14.6	-1.50 +0.052/-0.052	14.73	+5.075/-4.829	2.00 +0.691/-0.657
16.2	-1.10 +0.033/-0.033	11.00	+2.615/-2.570	1.50 +0.356/-0.350
16.4	-1.52 +0.058/-0.058	10.11	+5.545/-5.281	1.38 +0.754/-0.719
17.0	-1.50 +0.049/-0.049	15.64	+5.074/-4.822	2.13 +0.690/-0.656
34.8	-1.50 +0.052/-0.052	15.34	+5.487/-5.216	2.09 +0.747/-0.710
35.0	-1.20 +0.044/-0.044	3.81	+4.032/-3.893	0.52 +0.549/-0.530
35.2	-1.55 +0.044/-0.044	17.82	+5.955/-5.762	1.80 +0.602/-0.582
37.0	-0.91 +0.022/-0.022	12.08	+1.934/-1.867	2.14 +0.342/-0.330
38.0	-1.09 +0.035/-0.035	6.44	+2.669/-2.616	0.88 +0.363/-0.356
59.4	-1.22 +0.044/-0.044	6.82	+3.668/-3.503	0.93 +0.499/-0.477

Table A.2: Drag and upwelling flux predictions for trial 4 ($f = 0.52$ s^{-1}, $N = 4.4$ s^{-1}).

Time [s]	U_{sb} [cm s^{-1}]	Drag	[g cm s^{-2}]	Φ_{up} [cm^3 s^{-1}]
4.8	-1.10 +0.031/-0.031	11.04	+2.515/-2.469	1.50 +0.342/-0.336
7.4	-1.20 +0.044/-0.044	3.81	+4.032/-3.893	0.52 +0.549/-0.530
15.8	-1.09 +0.028/-0.028	10.93	+2.463/-2.416	1.49 +0.335/-0.329
16.8	-1.50 +0.049/-0.049	15.64	+5.074/-4.822	2.13 +0.690/-0.656
17.6	-1.10 +0.033/-0.033	11.00	+2.615/-2.570	1.50 +0.356/-0.350
23.4	-1.50 +0.053/-0.053	15.61	+5.162/-4.919	2.12 +0.702/-0.669
24.0	-1.50 +0.052/-0.052	14.73	+5.075/-4.829	2.00 +0.691/-0.657
25.6	-1.08 +0.036/-0.036	5.53	+2.814/-2.761	0.75 +0.383/-0.376
34.6	-1.09 +0.035/-0.035	6.44	+2.669/-2.616	0.88 +0.363/-0.356
35.8	-1.08 +0.036/-0.036	5.73	+2.737/-2.685	0.78 +0.372/-0.365
39.2	-1.22 +0.044/-0.044	6.82	+3.668/-3.503	0.93 +0.499/-0.477
46.8	-1.52 +0.058/-0.058	10.11	+5.545/-5.281	1.38 +0.754/-0.719
49.2	-1.50 +0.052/-0.052	15.34	+5.487/-5.216	2.09 +0.747/-0.710

Table A.3: Drag and upwelling flux predictions for trial 5 ($f = 0.40$ s^{-1}, $N = 2.2$ s^{-1}).

Time [s]	U_{sb} [cm s^{-1}]	Drag	[g cm s^{-2}]	Φ_{up} [cm^3 s^{-1}]
10.4	-1.50 +0.052/-0.052	14.73	+5.075/-4.829	2.00 +0.691/-0.657
13.8	-1.10 +0.031/-0.031	11.04	+2.515/-2.469	1.50 +0.342/-0.336
14.4	-1.50 +0.052/-0.052	15.34	+5.487/-5.216	2.09 +0.747/-0.710
15.6	-1.09 +0.035/-0.035	6.44	+2.669/-2.616	0.88 +0.363/-0.356
21.8	-1.50 +0.053/-0.053	15.61	+5.162/-4.919	2.12 +0.702/-0.669
34.4	-1.09 +0.028/-0.028	10.93	+2.463/-2.416	1.49 +0.335/-0.329
35.4	-1.20 +0.044/-0.044	3.81	+4.032/-3.893	0.52 +0.549/-0.530
50.6	-1.08 +0.036/-0.036	5.53	+2.814/-2.761	0.75 +0.383/-0.376
51.8	-1.50 +0.049/-0.049	15.64	+5.074/-4.822	2.13 +0.690/-0.656

Table A.4: Drag and upwelling flux predictions for trial 6 ($f = 0.70$ s^{-1}, $N = 2.2$ s^{-1}).

Time [s]	U_{sb} [cm s^{-1}]	Drag	[g cm s^{-2}]	Φ_{up} [cm^3 s^{-1}]
-12.6	-1.50 +0.049/-0.049	15.64	+5.074/-4.822	2.13 +0.690/-0.656
-7.2	-1.52 +0.058/-0.058	10.11	+5.545/-5.281	1.38 +0.754/-0.719
-1.0	-1.10 +0.031/-0.031	11.04	+2.515/-2.469	1.50 +0.342/-0.336
0.8	-1.50 +0.053/-0.053	15.61	+5.162/-4.919	2.12 +0.702/-0.669
6.2	-1.20 +0.044/-0.044	3.81	+4.032/-3.893	0.52 +0.549/-0.530
21.2	-1.09 +0.028/-0.028	10.93	+2.463/-2.416	1.49 +0.335/-0.329
21.8	-1.50 +0.052/-0.052	14.73	+5.075/-4.829	2.00 +0.691/-0.657
35.2	-1.08 +0.036/-0.036	5.53	+2.814/-2.761	0.75 +0.383/-0.376
65.6	-1.50 +0.052/-0.052	15.34	+5.487/-5.216	2.09 +0.747/-0.710
67.4	-1.09 +0.035/-0.035	6.44	+2.669/-2.616	0.88 +0.363/-0.356

Table A.5: Drag and upwelling flux predictions for trial 7 ($f = 0.52$ s^{-1}, $N = 2.2$ s^{-1}).

Time [s]	U_{sb} [cm s^{-1}]	Drag	[g cm s^{-2}]	Φ_{up} [cm^3 s^{-1}]
1.2	-1.09 +0.028/-0.028	10.93	+2.463/-2.416	1.49 +0.335/-0.329
3.6	-1.10 +0.031/-0.031	11.04	+2.515/-2.469	1.50 +0.342/-0.336
12.4	-1.09 +0.035/-0.035	6.44	+2.669/-2.616	0.88 +0.363/-0.356
19.2	-1.50 +0.053/-0.053	15.61	+5.162/-4.919	2.12 +0.702/-0.669
22.2	-1.08 +0.036/-0.036	5.53	+2.814/-2.761	0.75 +0.383/-0.376

Table A.6: Drag and upwelling flux predictions for trial 8 ($f = 0.52$ s^{-1}, $N = 2.2$ s^{-1}).